2015

Performance of full coverage effusion cooling with cross flow supply

Nathaniel Rogers

PERFORMANCE OF FULL COVERAGE EFFUSION COOLING
WITH CROSS FLOW SUPPLY

by

NATHANIEL ROGERS

A THESIS

Submitted in partial fulfillment of the requirements for the degree of
Master of Science in Engineering
in
The Department of Mechanical and Aerospace Engineering
to
The School of Graduate Studies
of
The University of Alabama in Huntsville

HUNTSVILLE, ALABAMA
2015

In presenting this thesis in partial fulfillment of the requirements for a master's degree from The University of Alabama in Huntsville, I agree that the Library of this University shall make it freely available for inspection. I further agree that permission for extensive copying for scholarly purposes may be granted by my advisor or, in his/her absence, by the Chair of the Department or the Dean of the School of Graduate Studies. It is also understood that due recognition shall be given to me and to The University of Alabama in Huntsville in any scholarly use which may be made of any material in this thesis.

Nathan Rogers   _12/18/2015_

(Student signature)   (Date)
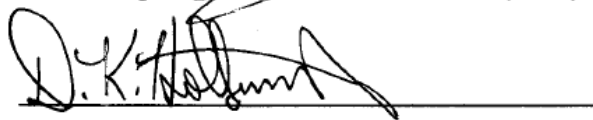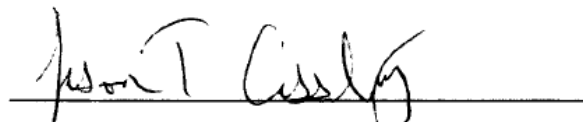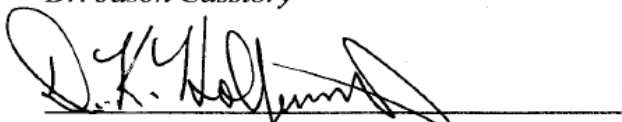
THESIS APPROVAL FORM

Submitted by Nathaniel Rogers in partial fulfillment of the requirements for the degree of Master of Science in Mechanical Engineering and accepted on behalf of the Faculty of the School of Graduate Studies by the thesis committee.

We, the undersigned members of the Graduate Faculty of The University of Alabama in Huntsville, certify that we have advised and/or supervised the candidate on the work described in this thesis. We further certify that we have reviewed the thesis manuscript and approve it in partial fulfillment of the requirements for the degree of Master of Science in Mechanical Engineering.

_____ Committee Chair
Dr. Phillip Ligrani   (Date)

_____
Dr. Keith Hollingsworth

_____
Dr. Jason Cassibry

_____ Department Chair
Dr. Keith Hollingsworth

_____ College Dean
Dr. Shankar Mahalingam

_____ Graduate Dean
Dr. David Berkowitz

ABSTRACT
The School of Graduate Studies
The University of Alabama in Huntsville

Degree___Master of Science in Engineering___   Program___Mechanical Engineering___
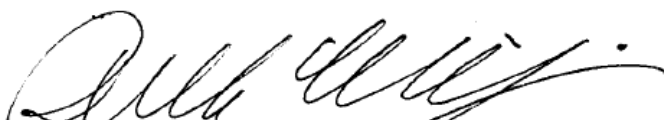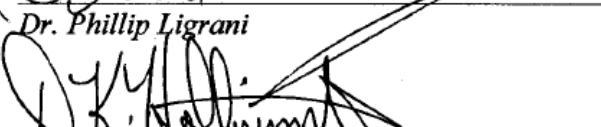
Name of Candidate_____Nathaniel D. Rogers_____

Title_____Performance of Full Coverage Effusion Cooling with Cross Flow Supply_____

Experimental results are presented for a double wall cooling arrangement which simulates a portion of a combustor liner of a gas turbine engine. The results are collected using a new experimental facility designed to test full coverage film cooling and impingement cooling effectiveness using either cross flow, impingement, or a combination of both to supply the film cooling flow. The present experiment primarily deals with cross flow supplied full coverage film cooling for a sparse film cooling hole array that has not been previously tested. Data are provided for turbulent film cooling, contraction ratio of 1, blowing ratios ranging from 2.78 to 4.94, coolant Reynolds numbers based on film cooling hole diameter of 7,000 – 12,000, and mainstream temperature step during transient tests of 7 ℃ to 10 ℃. The film cooling hole array consists of a film cooling hole diameter of 6.4 mm with non-dimensional streamwise (X/d_e) and spanwise (Y/d_e) film cooling hole spacing of 15 and 4, respectively. The film cooling holes are streamwise inclined at an angle of 25 degrees with respect to the test plate surface and have adjacent streamwise rows staggered with respect to each other. Data illustrating the effects of blowing ratio and main flow velocity on adiabatic film cooling effectiveness and heat transfer coefficient are presented. For the arrangement and conditions considered, heat transfer coefficients generally increase with streamwise development, and increase with increasing blowing ratio. The adiabatic film cooling effectiveness is determined from measurements of adiabatic wall temperature, coolant stagnation temperature, and mainstream recovery temperature. The adiabatic wall temperature and adiabatic film cooling effectiveness generally decrease and increase, respectively, with streamwise position, and generally decrease and increase, respectively, as blowing ratio becomes larger.

Abstract Approval: Committee Chair _____
                                                            Dr. Phillip Ligrani
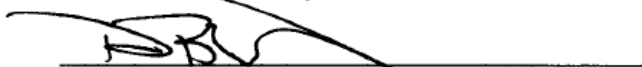
                                             Department Chair _____
                                                            Dr. Keith Hollingsworth

                                             Graduate Dean _____
                                                            Dr. David Berkowitz

iv

ACKNOWLEDGEMENTS

TABLE OF CONTENTS

LIST OF FIGURES

LIST OF TABLES

LIST OF SYMBOLS

A	impingement hole area
A_{cs}	cross-sectional area of duct
A_{or}	orifice area
A_e	cross-sectional area of each film cooling hole
A_i	cross-sectional area of each impingement hole
BR	film cooling blowing ratio
C	Sutherland's formula constant
C_d	discharge coefficient
c	specific heat
D_H	hydraulic diameter
d_e	film cooling hole diameter
d_i	impingement hole diameter
h	heat transfer coefficient
$\bar{h}$	line-averaged heat transfer coefficient
K	flow coefficient
k	thermal conductivity
M	Mach number
$\dot{m}$	mass flow rate
N_e	number of holes in the film cooling test plate
N_i	number of holes in the impingement plate
ΔP_e	differential pressure through film cooling plate
ΔP_i	differential pressure through impingement plate
ΔP_{or}	differential pressure through ASME orifice plate
P_s	static pressure
P_d	dynamic pressure
P_t	stagnation pressure
$\dot{q_o}''$	wall heat flux

R	gas constant
Re	Reynolds number
T_{aw}	adiabatic wall temperature
$\overline{T_{aw}}$	line-averaged adiabatic wall temperature
T_{surf}	surface/wall temperature
T_i	initial temperature
T_r	thermocouple recovery temperature
T_s	static temperature
T_t	stagnation temperature
T_0	reference static temperature
t	time
V	flow velocity
x	streamwise coordinate
X	streamwise film hole spacing
y	spanwise coordinate
Y	spanwise film hole spacing
z	surface normal coordinate
Δz	polystyrene thickness

Greek symbols

α	thermocouple recovery factor
β	diameter ratio
γ	specific heat ratio
η	adiabatic film cooling effectiveness
$\bar{\eta}$	line-average adiabatic film cooling effectiveness
μ	dynamic viscosity
μ_0	reference dynamic viscosity
ρ	density
ρ_s	static air density

Subscripts

C	cross flow film cooling supply channel
e	film cooling plate
I	impingement supply channel
i	impingement plate
M	main flow supply channel
or	orifice plate
P	impingement plenum
Avg	average values along test plate
Local	local values along test plate

CHAPTER 1

INTRODUCTION

1.1 Overview

Full coverage film cooling provides a layer of protective coolant fluid over surfaces exposed to gas at elevated temperatures. The coolant is injected into the boundary layer of the hot gas and creates a film which acts as a heat sink and an insulator for the protected surface. This process reduces the heat load transferred to the surface (see Fig. 1). Film cooling is currently employed in a variety of high temperature applications, including turbine blades and combustor liners of gas turbine engines. The present study is undertaken using a unique experimental facility which has been designed and assembled at the Propulsion Research Center of the University of Alabama in Huntsville especially for the present investigation. The purpose of the present research is to provide new heat transfer data for film cooling using a sparse hole array that has not been previously investigated. New data are presented, which illustrate the capabilities of this new double wall cooling test facility, and illustrate the performance of a sparse effusion hole array which is supplied by a cross flow channel.
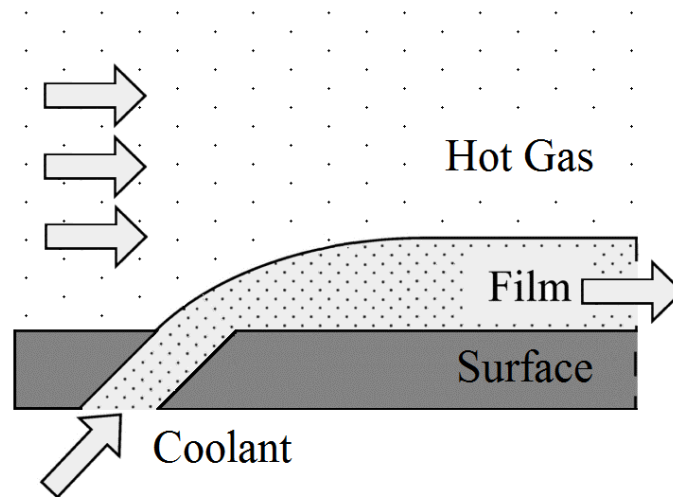
Figure 1. Example film cooling diagram.

1.2 Literature Survey

Recent previous investigations consider film cooling with hole arrays [1-4]. Other recent film cooling investigations are described by Baldauf et al. [5,6], Bell et al. [7], Yuen and Martinez-Botas [8], Coulthard et al. [9], Saumweber et al. [10], and Chappell et al. [11,12]. In general, each study considers the effects of different hole configurations, hole inclination angles, hole orientation angles, mainstream pressure gradients, blowing ratios, temperature ratios, density ratios, and freestream turbulence intensities on surface adiabatic film cooling effectiveness and surface heat transfer coefficients. Most of these studies indicate that the effectiveness for blowing ratios decreases above 0.5 for round holes. This is because increased jet momentum (with respect to the freestream mass flux) generates liftoff, where the cooling fluid separates from the film-cooled surface. The protrusion of the jet into the freestream then generates vortices which move hot fluid from the freestream directly into contact with the cooled surface beneath the film. Lin et al. [13] show that, for a range of blowing ratios from 1 to 4 and dense hole spacings of X/d_e=8, Y/d_e=4 and X/d_e=5.67, Y/d_e=5.67, holes inclined in the direction of the freestream show negligible performance change with increasing blowing ratio. Blowing ratio values in the inclined multi-hole liner of a gas turbine combustor generally range from 2 to 10. Other recent, related film cooling investigations, including ones devoted to combustor liner cooling, are discussed by Schulz [14], Bailey et al. [15], Amano [16], and Bunker [17]. A recent experimental double wall cooling investigation is described by Cho and Rhee [18]. Within this study, mass transfer rate results are measured using a naphthalene sublimation technique. Double wall cooling investigations which employ numerical prediction approaches are undertaken by King and Jagannatha [19] and Kumar et al. [20]. Barigozzi et al. [21] consider the effects of effusion cooling through non-cylindrical holes.

The present study is undertaken using a unique experimental facility which is designed and assembled at the Propulsion Research Center of the University of Alabama in Huntsville especially for the present investigation. The facility uses three independent flow channels to provide double wall cooling arrangements which model the same configurations from operating gas turbine engines (see Fig. 4). The facility is designed to provide full coverage film cooling data and impingement cooling effectiveness data, wherein the film cooling flow is supplied using either cross flow, impingement flow, or a combination of both together. As such, new data are presented,

which illustrate the capabilities of this new double wall cooling test facility, and illustrate the performance of a sparse effusion hole array which is supplied by a cross flow channel.
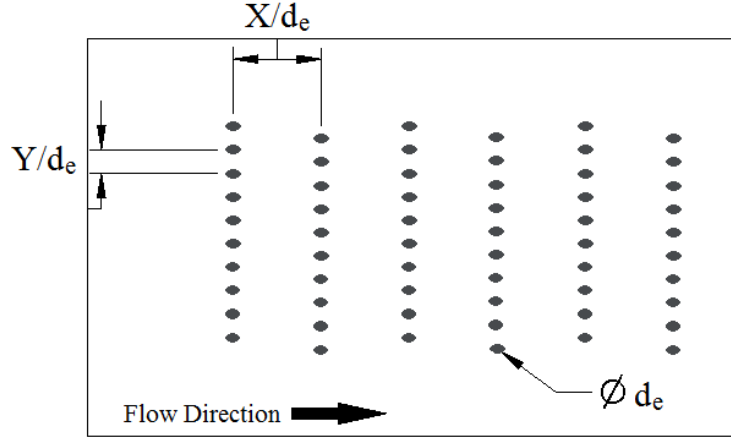
Figure 2. Example test plate surface showing the d_e, X/d_e, and Y/d_e measurement locations.

Recent studies by Ligrani et al. [1,2] are different from the present investigation, since they use only a single source plenum supply for the film cooling array, and provide data for only the film cooled side of the test plate. The present test facility provides more realistic experimental data to model complex three-dimensional flow and heat transfer interactions, and has the capability to provide spatially-resolved data for both sides (hot side and cold side) of the film cooling test plate. Within the present paper, data are given with a cross flow supply for the film cooling air, with data provided for the film cooled surface (or hot side) of the effusion test plate. Considered is a sparse hole array, with non-dimensional streamwise (X/d_e) and spanwise (Y/d_e) film cooling hole spacings of 15 and 4, respectively (see Fig. 2). Note that the Ligrani et al. [1] study considers a sparse hole array with non-dimensional streamwise (X/d_e) and spanwise (Y/d_e) film cooling hole spacings of 18 and 5, respectively. In the present investigation, experimental data are obtained for full-coverage film cooling with main flow air velocities of 5, 7 and 9 m/s. For each main flow velocity, the overall, spatially-averaged blowing ratio is varied from 2.8 to 4.9. The mainstream flow passage contraction ratio is 1 for all tests. Within the film cooling hole array, the hole diameter is 6.4 mm. The film cooling holes are streamwise inclined at an angle of 25 degrees with respect to the test plate surface and have adjacent streamwise rows staggered with respect to each other. The film is turbulent for all experimental conditions investigated. Of particular interest are the effects

of blowing ratio, mainstream flow velocity, and mainstream flow static temperature on spatially-resolved distributions of adiabatic film cooling effectiveness and heat transfer coefficient.

The resulting data are useful for design of gas turbine components, as well as for the development and validation of codes for numerical prediction of such component flows. The channel and effusion cooling arrangement, including the sparse hole arrangement, and associated experimental conditions are new, and as such, are different from any previous investigation.

1.3 Non-dimensional Parameters

The Reynolds number is the ratio of momentum forces to viscous forces, and it is used to characterize a flow regime as laminar, transitional, or turbulent. The molecular Prandtl number is the ratio of momentum diffusivity to thermal diffusivity of a fluid. The molecular Prandtl number for air in the temperature range of this experiment is 0.71. The turbulent Prandtl number is the ratio of momentum eddy diffusivity to heat transfer eddy diffusivity. The Nusselt number is the ratio of convective to conductive heat transfer from a fluid across a boundary. The Stanton number is the ratio of heat transferred into a fluid to the thermal capacity of the fluid, and is used to characterize heat transfer in forced convection flows. The Biot number is defined as the ratio of heat transfer resistance inside a solid body to heat transfer resistance at the interface of a solid body and a fluid, and is used to characterize the thermal gradients inside a solid body based on thermal gradients applied at a surface. The Biot number appears in the solution to Fourier's Law used for this experiment (Eq. (25)). The blowing ratio is defined as the ratio of the coolant mass flux to the mainstream mass flux at the test plate. The blowing ratio is used to characterize and compare effusion cooling flows. The parameters considered within the present study include Reynolds number, Prandtl number, and Biot number.

1.4 Organization of the Thesis

This thesis is composed of four chapters, seven appendices, and a reference list. The experimental apparatus and procedures section presented in Chapter 2 describes the new experimental test facility in detail, and provides the measurement and analysis procedures for the experiment. Portions of the material in this section are taken from Ligrani, et al. [1]. The experimental results section presented in Chapter 3 presents new experimental data for the specified test conditions and sparse hole array investigated, including surface plots, local line plots,

and spatially-averaged line plots for heat transfer coefficient, adiabatic wall temperature, and adiabatic film cooling effectiveness. Chapter 4 presents a summary and conclusion of the thesis. Appendix A presents a range of test conditions achieved by the test facility. Appendix B presents an uncertainty analysis. Appendix C presents details of the *in situ* infrared calibration. Appendix D presents information about improvements to the facility designed to eliminate ground loop contamination. Appendix E presents details of the experimental apparatus and procedures used in the present investigation. Appendix F presents a software directory. Appendix G presents a data file directory.

CHAPTER 2

EXPERIMENTAL APPARATUS AND PROCEDURES

The apparatus and procedures of the double wall cooling experimental facility at the University of Alabama in Huntsville Propulsion Research Center are presented. Included are all relevant measurement details related to the present experimental investigation.

2.1 Double wall cooling test facility

Schematic diagrams of the facility used for the present study, including measurement details, are presented in Figs. 3-12. The facility (Fig. 3) consists of a double wall cooling test section (Fig. 4) and the equipment employed to supply properly conditioned air for the mainstream flow, the cross flow supply flow, and the impingement flow. As mentioned, the film cooling air is supplied by impingement jets from the impingement plate, by a cross flow arrangement, or by a combination of both. The impingement air is supplied by a plenum arrangement. The hot mainstream flow is supplied by an inlet and flow management apparatus.
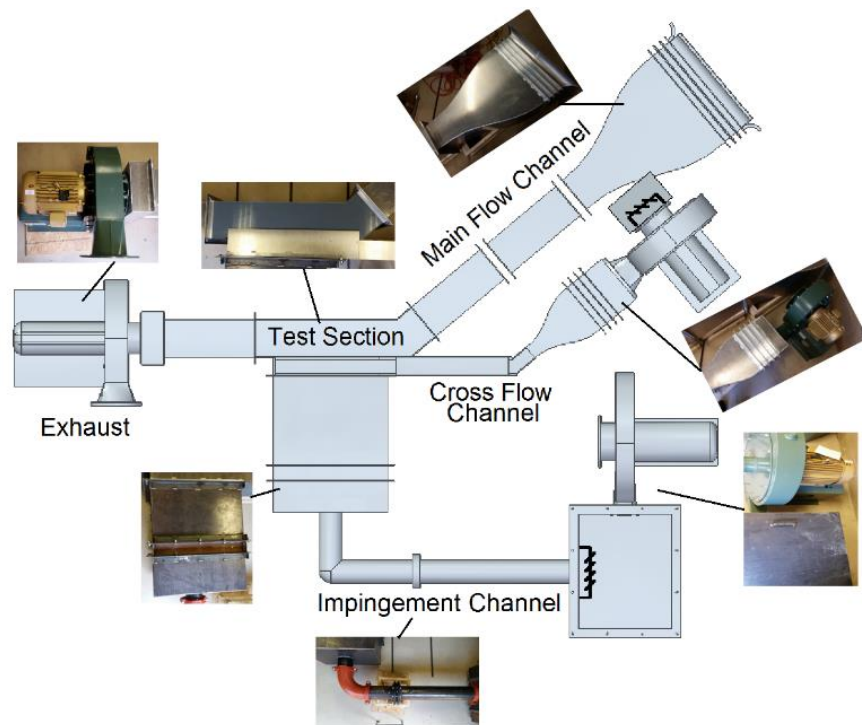
Figure 3. Experimental test facility, with all components.

Figure 3 shows a total view of the test facility with photographs of specific components. The main flow channel consists of a bell mouth inlet, a nozzle, a straight duct with two mesh heaters, the test section, an exhaust plenum with a baffle, and a blower. Attached to the bell mouth inlet are flow straightening devices, including a honeycomb and screens. The nozzle has a two-dimensional, fifth-order polynomial geometry. Airflow is induced through the mainstream channel by means of suction, which is generated at the exit for the flow stream, by a New York Blower Co. 1708A pressure blower with a 15 HP 1800 RPM motor. The blower is controlled by a Fuji Electric 15 HP three-phase variable frequency drive. Excluding the blower, the main flow channel is constructed of aluminum.

The two mesh heaters are composed of Kanthol-D wire mesh, and are connected in series to an Ametek Sorensen SGA60/500D 30 kilowatt DC power supply. The mesh heaters are thermally and electrically isolated from the facility using multiple 12 mm thick Teflon frames. After passing through the heater mesh, the bulk flow enters the working section where it encounters a constant area duct. It then enters a transition duct and passes into the blower.

The cross flow supply channel consists of a heat exchanger, a blower, a plenum, a nozzle, a duct, and the test section. The heat exchanger is attached to the blower inlet, and uses liquid nitrogen to cool the air as it enters into the blower. The channel inlet is connected to the high pressure side of the blower. This blower is a New York Blower Co. 1808S device, with a 7.5 HP 1800 RPM motor. The blower is controlled by a Fuji Electric 7.5 HP three phase variable frequency drive. Inside the plenum are flow straightening devices, including a baffle, honeycomb and screens. The nozzle has a two-dimensional, fifth-order polynomial geometry. Excluding the blower, the cross flow channel is constructed of aluminum.

The impingement supply consists of a blower, an upstream plenum, a flow measurement pipe, and a downstream plenum, which leads to the test section. The blower is a 2404A pressure blower with a 15 HP 1800 RPM motor. The pressure side of the blower is connected to the plenum which follows. The blower is controlled by a Fuji Electric 15 HP three phase variable frequency drive. The upstream plenum contains a heat exchanger. Liquid nitrogen is employed to cool the air stream within this device. An ASME orifice plate is used to measure the mass flow rate of the air in the flow measurement pipe. The downstream plenum contains flow straightening devices,

including a baffle, honeycomb and screens. Excluding the blower, the impingement channel is constructed of steel.
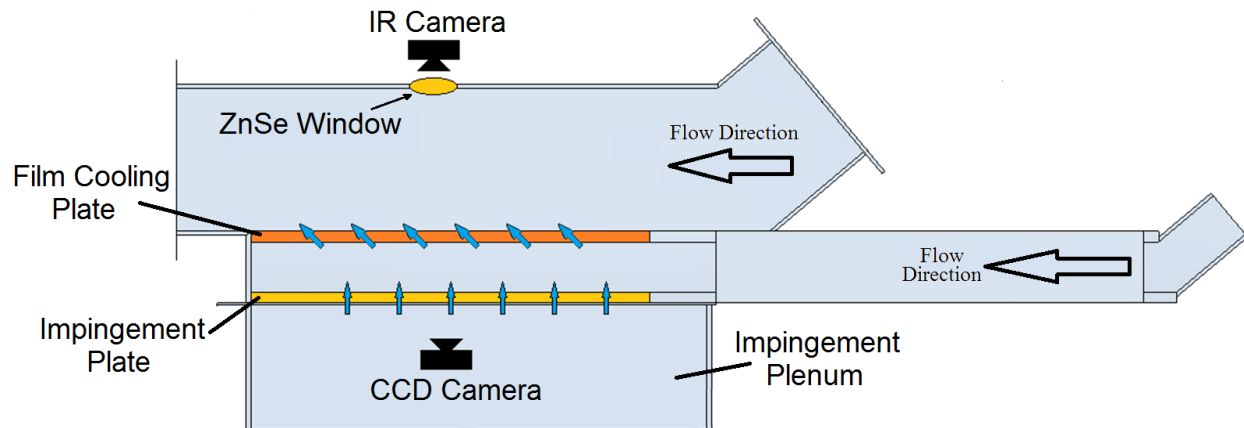
Figure 4. Cross-sectional view of the double wall cooling test section, including optical instrumentation arrangements.

2.2 Test section and test surfaces

Figure 4 shows a side, cross-sectional view of the test section, including optical instrumentation arrangements. Overall, the test section consists of a frame structure, a main flow channel, a cross flow channel, an impingement plenum, a film cooling test plate, an impingement test plate, associated attachment components, and other associated components. The main flow channel directs the hot main flow air across the exit side of the film cooling test plate. Another main flow channel structure is also available with a contraction ratio, which can be employed to create a pressure gradient along the test plate. The height of the main flow shell is 254 mm from the test plate surface. The cross flow channel directs air flow across the entrance side of the film cooling test plate. A plenum mount connects the test section to the impingement supply plenum. Note that the impingement plate and the film cooling plate are both removable, allowing installation of different plates for testing different hole configurations.
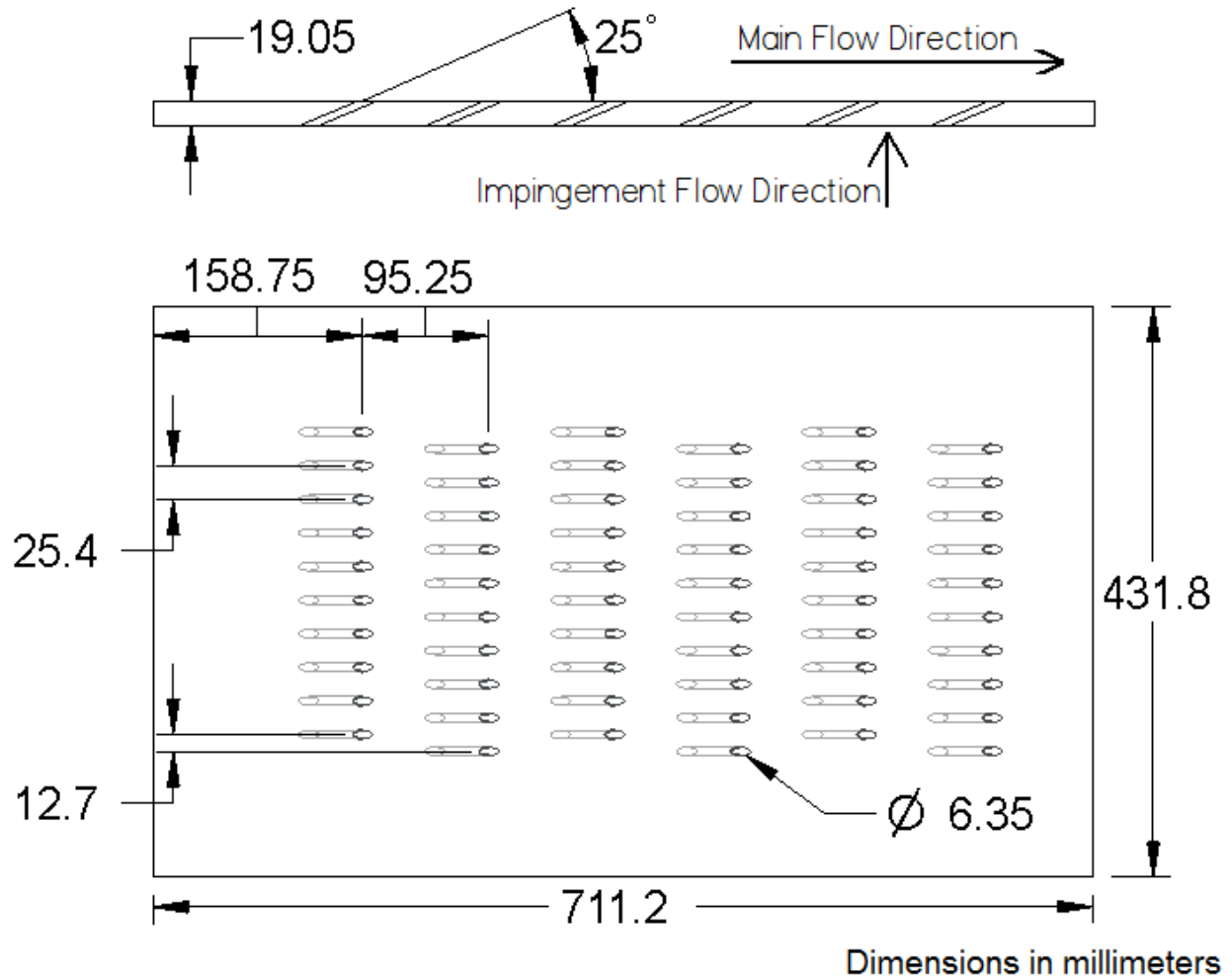
Figure 5. Film cooling test plate.

The film cooling test plate is shown in Fig. 5 and contains holes that direct cooling air from the supply area onto the surface adjacent to the mainstream flow to create a film cooled layer along the surface of the test plate. Each face of the film cooling test plate contains thermocouples embedded between a 1.5 mm thick polystyrene sheet and the PVC plastic core. On the cool side of the film cooling test plate, a thin film heater is also included between the PVC core and the polystyrene sheet, to provide a constant heat flux thermal boundary condition. As such, the test plate is constructed from 16 mm thick PVC type 1 plastic with thermal conductivity of approximately 0.17 W/mK. Each 1.5 mm thick polystyrene sheet has thermal conductivity of approximately 0.22 W/mK. The test plate contains 60 holes arranged in 6 offset columns of 10 holes each. Streamwise (X/d_e) and spanwise (Y/d_e) hole spacings are 15 and 4, respectively. The

columns are spaced 95.3 mm apart, the holes in each column are 25.4 mm apart, and every other column is offset 12.7 mm. Each hole has a diameter of 6.4 mm and is cut at an angle of 25° relative to the surface of the test plate. The entire test plate is 431.8 mm in the spanwise direction, and 711.2 mm in the streamwise direction. The first column of holes exits the main flow side of the test plate 158.8 mm from the start of the plate. Note that the flow develops down the length of the test section, and there is no flow trip used in this experiment.
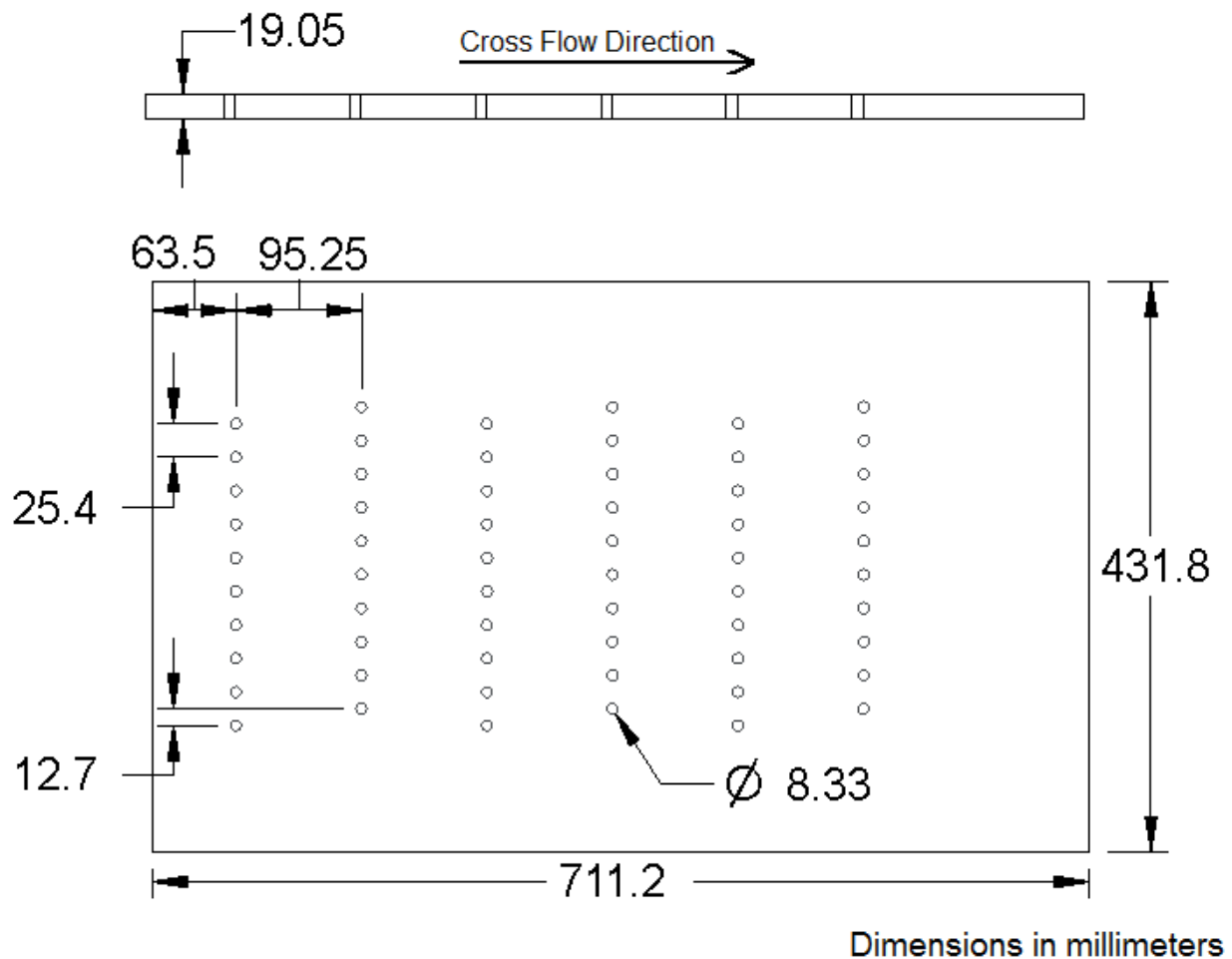
Figure 6. Impingement test plate.

Figure 6 is a detailed drawing of the impingement plate. This plate contains holes that direct jets of air from the impingement supply plenum into a target surface, which is comprised of the cool side of the film cooling test plate. The impingement plate is made of 19 mm thick, optically-transparent acrylic. The plate contains 60 holes arranged in 6 offset columns of 10 holes each. The

columns are spaced 95.3 mm apart, the holes in each column are 25.4 mm apart, and every other column is offset 12.7 mm. Each hole has a diameter of 8.3 mm and is oriented at an angle of 90° relative to the surface of the plate. The entire plate is 431.8 mm in the spanwise direction, and 711.2 mm in the streamwise direction. The first column of holes exits the plate 63.5 mm from the start of the plate.
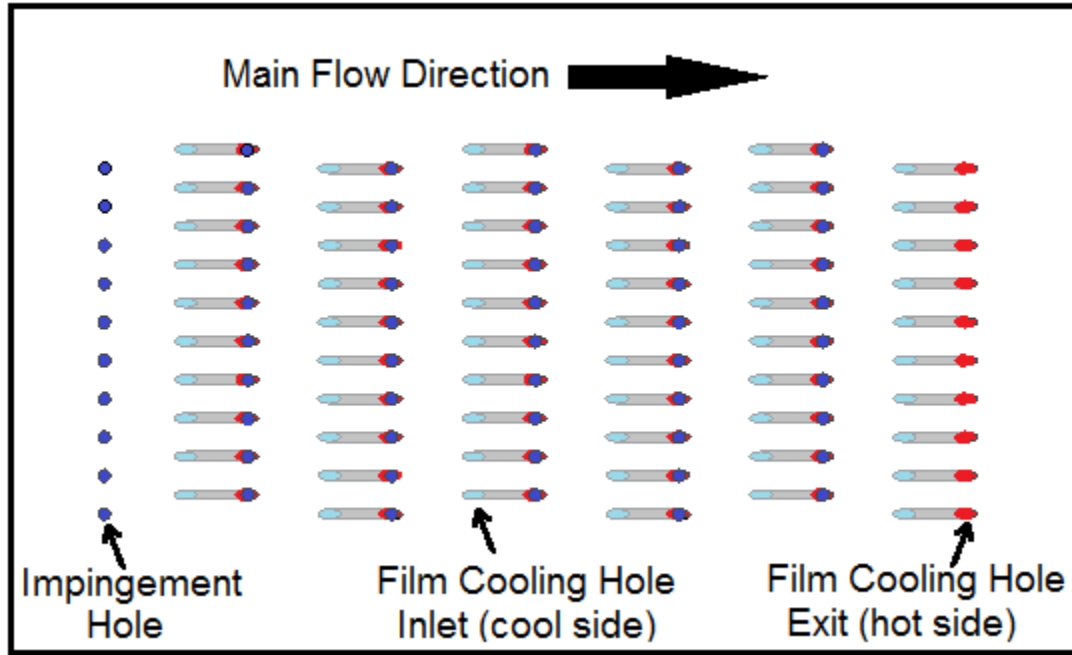
Figure 7. Film cooling and impingement test plates, with relative hole locations.

Figure 7 shows the relative arrangement of the impingement and film cooling plates, with the relative locations of the associated sets of holes. The impingement holes are arranged so that each impingement jet strikes the cool side of the film cooling plate midway between film cooling hole entrances (in both streamwise and spanwise directions).
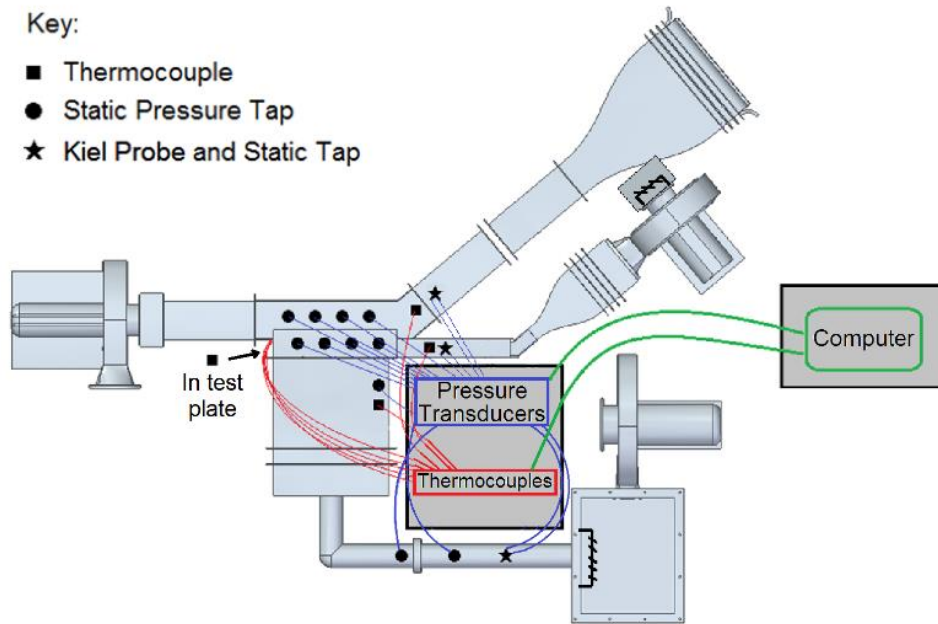
Figure 8. Experimental test facility, with temperature and pressure measurement locations.

2.3 Flow temperature, pressure, density, mass flow rate, and velocity measurements

Figure 8 shows the instrumentation for the entire facility. Temperature measurements are made with Omega 5TC-TT-T-40-72 fine-wire copper-constantan (Type T) thermocouples. When located within an air stream, each thermocouple wire (leading to the junction) is directed parallel to the flow. The associated recovery factor α is 0.86. Thermocouple signals are acquired at a rate of 2.0 Hz using two National Instruments NI 9213 thermocouple input cards mounted within a National Instruments NI cDAQ-9188 chassis connected to the computer workstation.

Pressure is measured using wall static pressure taps and United Sensor Corporation KCC-8 Kiel probes. The static taps consist of a 1.59 mm hole drilled through the facility wall, a 6.35 mm metal tube on the exterior of the facility wall, and 6.35 mm tubing to carry the pressure signal. Each Kiel probe head is located in the center of the flow channel, and is connected to 3.18 mm tubing to carry the pressure signal. Dynamic pressure is the difference between the stagnation pressure measured using the Kiel probe and static pressure measured using the wall pressure taps. To minimize uncertainty associated with these measurements, each Kiel probe is carefully aligned with the flow in each channel. Such alignment involves stagnation pressure measurement as the probe tip is rotated, where correct alignment coincides with maximum local stagnation pressure. Pressure signals are measured using Validyne DP15 differential pressure transducers connected to Validyne

CD15 Carrier Demodulators. Each Carrier Demodulator is modified to include a 100 microfarad capacitor across the output terminals to suppress environmental noise effects, which are especially important when signal levels are relatively small. The signals from the Carrier Demodulators are acquired at a rate of 2.0 Hz using a National Instruments NI USB-6210 data acquisition card, connected to the computer workstation.
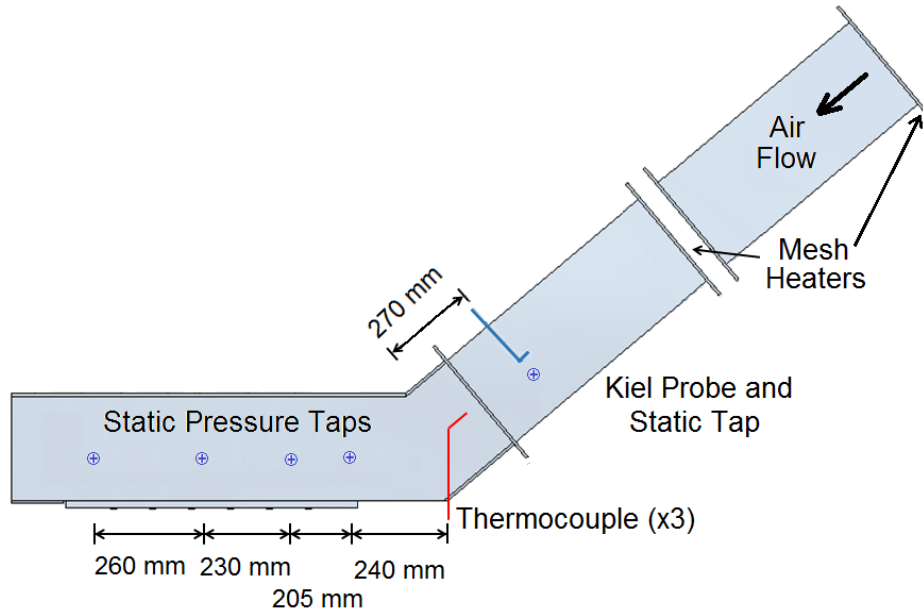
Figure 9. Instrumentation for mainstream flow channel.

Figure 9 shows instrumentation arrangements for the main flow channel. Four static pressure taps are located along the side wall of the test section. Three thermocouples are located just upstream of the test section inlet to measure the recovery temperature of the main flow air. A Kiel probe and static pressure tap are also located just upstream of the test section entrance to measure dynamic pressure. Also shown in Fig. 9 are the locations of the two mesh heaters used to generate a step increase in air flow temperature of the mainstream air. Measured magnitudes of mainstream stagnation pressure and mainstream static pressure give an approximately linear variation of streamwise freestream velocity with streamwise distance. The local freestream static temperature also varies with streamwise location, but by only small amounts, in accordance with streamwise changes of freestream velocity, freestream dynamic temperature, and freestream stagnation temperature, which is constant. Such parameters are then also used to determine local values of freestream static density, and freestream velocity.
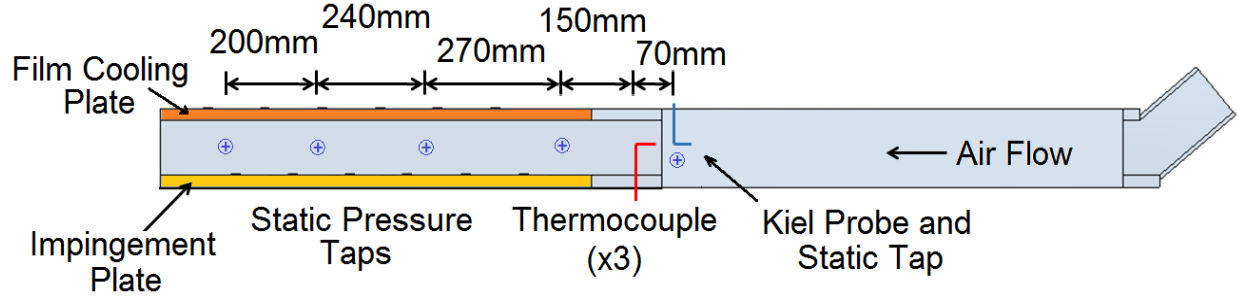
Figure 10. Instrumentation for cross flow supply channel.

Figure 10 shows the instrumentation for the cross flow supply channel. Four static pressure taps are located in the film cooling supply area of the duct. Three thermocouples are located just upstream of the duct entrance (also just upstream of the test section) to measure the recovery temperature of the cross flow supply air. A Kiel probe and static pressure tap are also located just upstream of the duct entrance to measure dynamic pressure.
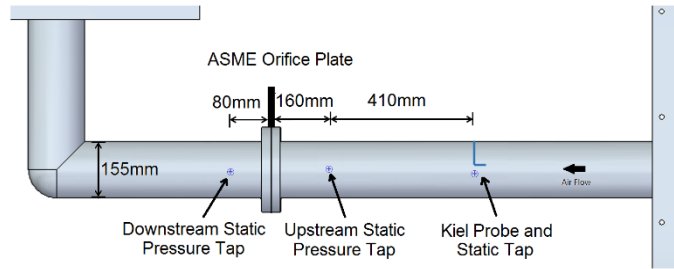
Figure 11. Instrumentation for impingement supply passage.

Figure 11 shows instrumentation for the impingement supply channel. This impingement supply channel is connected to the impingement supply plenum. Within the supply channel, an ASME standard orifice plate is used to measure the total air mass flow rate within the channel. To accomplish this task, two static pressure taps are located 1 diameter upstream and ½ diameter downstream of the orifice plate. The orifice plate for the present investigation is manufactured with a diameter ratio β of 0.5. To determine the mass flow rate through the orifice plate, the following equation is employed

$$\dot{m}_{or} = \dot{m}_I = K A_{or} \sqrt{2\rho_{s,I}\Delta P_{or}} \tag{1}$$

Here, the flow coefficient is initially assumed to be $K = 0.62$. Next, the orifice plate Reynolds number is determined using the flow measurement pipe diameter as the hydraulic diameter, and a new value for the flow coefficient is determined using ASME orifice plate data. These calculations are then repeated in an iterative fashion to ultimately determine the true mass flow rate through the orifice plate. Note that a redundant flow rate determination is performed for each measurement condition using a Kiel probe and a wall static pressure tap, which are located within the duct, upstream of the orifice plate.
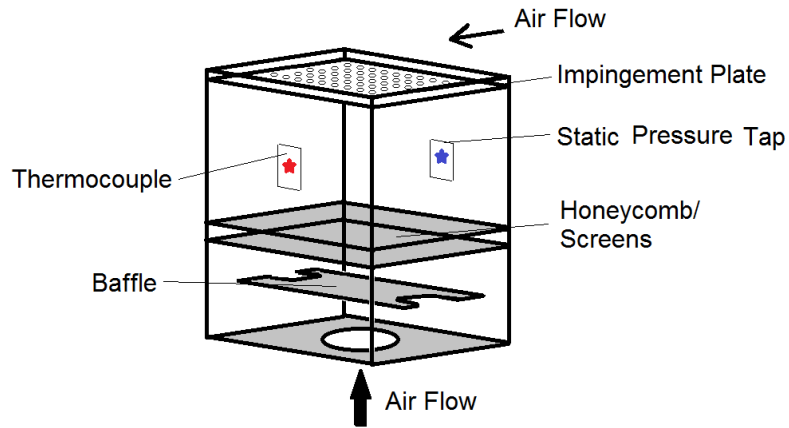
Figure 12. Instrumentation for impingement supply plenum.

The instrumentation for this supply plenum is illustrated by Fig. 12. Here, a thermocouple is used to measure plenum air stagnation temperature, and several wall static pressure taps are used to measure the plenum static pressure. The air in the plenum is effectively stagnant because the cross sectional area of the plenum in the direction of flow is much larger than the flow area of the impingement plate holes. This plenum also serves as a mounting location for the CCD camera, which is employed for thermal imaging of the cool side of the film cooling test plate, as shown in Fig. 4.

The difference in pressure between the film cooling supply chamber and the local test section static condition is measured between the film cooling source chamber and four points along the contraction. Unlike the freestream velocity, this difference does not vary linearly with streamwise distance along the contraction. A curve-fitting routine is therefore applied to determine the static pressure difference between the film cooling source chamber and the local freestream flow for each streamwise row of holes. This difference, and the resulting pressure ratio are then utilized in determining the discharge coefficient for the film hole array, as well as local film cooling injection

15

velocity, V_e, and local film static density, $\rho_{s,e}$. The four locations for measurement of the freestream static pressure through the test section are shown in Fig. 9.

LABVIEW commercial software is used to control the acquisition of data from the thermocouples and pressure transducers during each test run. Air static density is determined using the ideal gas equation. The Bernoulli equation is used to calculate the air velocity, assuming constant density conditions. Local air stream static temperature is determined from measurements of flow velocity and thermocouple-measured recovery temperature, using the equation given by

$$T_s = T_r - \alpha * (V^2/2c) \tag{2}$$

where α is the recovery factor. The viscosity of the air is determined using Sutherland's formula

$$\mu = \mu_0 \frac{T_0+C}{T_s+C} \left(\frac{T_s}{T_0}\right)^{3/2} \tag{3}$$

where $C = 120$, $T_0 = 291.15$ K, and $\mu_0 = 1.827\text{E-}5$ Pa-s.

2.4 Impingement flow conditions and parameters determination

The static density of the impingement jets is determined using the ideal gas equation of state. Next, the impingement jet velocity is determined using the equation given by

$$V_i = \frac{\dot{m}_I}{\rho_{s,i} A_i N_i} \tag{4}$$

Impingement jet static temperature is then calculated using the equation given by

$$T_{s,i} = T_{t,P} - \frac{V_i^2}{2c} \tag{5}$$

Here, stagnation temperature is initially set equal to the temperature in the impingement supply plenum. Equations (4), (5), and related equation of state relationships are then iterated to obtain the correct values for impingement jet static density, spatially-averaged velocity, and static temperature. Next, the viscosity of the air is calculated using Eqn. (3). For the next steps, the

discharge coefficient, Reynolds number, and average Mach number are determined using the following respective relationships

$$C_{d,i} = \frac{(\rho_{s,i}V_i)_{Avg}}{(\rho_{s,i}V_i)_{Ideal}} = \frac{\dot{m}_I/A_iN_i}{\sqrt{2\rho_{s,i}(\Delta P_{i,Avg})}} \tag{6}$$

$$Re_{i,Avg} = \frac{d_i}{\mu_i}(\rho_{s,i}V_i)_{Avg} = \frac{d_i}{\mu_i}\frac{\dot{m}_I}{A_iN_i} \tag{7}$$

$$M_{i,Avg} = \frac{V_{i,Avg}}{\sqrt{\gamma RT_{s,i}}} = \frac{V_i}{\sqrt{\gamma RT_{s,i}}} \tag{8}$$

Because multiple static pressure taps are located along the cross flow supply channel, which is adjacent to the test section, local values for Reynolds number and Mach number are determined using equations with the following forms

$$Re_{i,Local} = \frac{d_i}{\mu_i}(\rho_{s,i}V_i)_{Local} = \frac{d_i}{\mu_i}C_{d,i}\sqrt{2\rho_{s,i}\Delta P_{i,Local}} \tag{9}$$

$$M_{i,Local} = \frac{V_{i,Local}}{\sqrt{\gamma RT_{s,i}}} = \frac{C_{d,i}\sqrt{2\Delta P_{i,Local}}}{\sqrt{\rho_{s,i}}\sqrt{\gamma RT_{s,i}}} \tag{10}$$

With this approach, local mass flow rate, spatially-averaged velocity, Reynolds number, and Mach number are determined for each streamwise row of impingement holes.

2.5 Film cooling flow conditions and parameters determination

The mass flow rate for the film cooling is the sum of the mass flow rate for the cross flow supply and the mass flow rate for the impingement supply

$$\dot{m}_e = \dot{m}_C + \dot{m}_I \tag{11}$$

The stagnation temperature for the film cooling is the mass weighted average of stagnation temperatures of the cross flow supply flow and impingement supply flow, as given by

$$T_{t,e} = \frac{T_{t,C}\dot{m}_C + T_{t,I}\dot{m}_I}{\dot{m}_e} \tag{12}$$

The static density of the film coolant is determined using the ideal gas equation of state, where the film cooling static temperature is initially assumed to be equal to the stagnation temperature in the film cooling supply flow. Next, the film cooling flow velocity is determined using an equation of the form

$$V_e = \frac{\dot{m}_e}{\rho_{s,e} A_e N_e} \tag{13}$$

An iterative analysis approach is then employed to determine temperatures which satisfy Eqn. (13) and the associated equation of state relationships. The static temperature is iteratively calculated using Eqn. (5) and the film cooling flow velocity. The static density is iteratively calculated using the ideal gas equation of state and the static temperature. Finally, a new film cooling flow velocity is calculated using Eqn. (13) and the static density. The iteration terminates when the static temperature value converges to within 0.01 percent. Upon completion of this process, correct values for film cooling flow static density, velocity, and static temperature are determined. Next, the viscosity of the air is calculated using Eqn. (3). This is followed by determination of the discharge coefficient, blowing ratio, Reynolds number, and Mach number (where each quantity is spatially-averaged for all film cooling holes), as given by

$$C_{d,e} = \frac{(\rho_{s,e}V_e)_{Avg}}{(\rho_{s,e}V_e)_{Ideal}} = \frac{\dot{m}_e/A_e N_e}{\sqrt{2\rho_{s,e}(\Delta P_{e,Avg})}} \tag{14}$$

$$BR_{e,Avg} = \frac{(\rho_{s,e}V_e)_{Avg}}{(\rho_{s,M}V_M)_{Avg}} = \frac{\dot{m}_e/A_e N_e}{\rho_{s,M}V_M} \tag{15}$$

$$Re_{e,Avg} = \frac{d_e}{\mu_e}(\rho_{s,e}V_e)_{Avg} = \frac{d_e}{\mu_e}\frac{\dot{m}_e}{A_e N_e} \tag{16}$$

$$M_{e,Avg} = \frac{V_{e,Avg}}{\sqrt{\gamma R T_{s,e}}} = \frac{\dot{m}_e/\rho_{s\,e}A_eN_e}{\sqrt{\gamma R T_{s,e}}} \tag{17}$$

The blowing ratio is the ratio of local film cooling mass flux to local mainstream mass flux. By using measured distributions of static pressure measured along the main flow test section, local values of blowing ratio, Reynolds number, and Mach number are calculated by utilizing the following equations

$$BR_{e,Local} = \frac{(\rho_{s,e}V_e)_{Local}}{(\rho_{s,M}V_M)_{Local}} = \frac{C_{d,e}\sqrt{2\rho_{s,e}\Delta P_{e,Local}}}{\sqrt{2\rho_{s,M}P_{d,M,Local}}} \tag{18}$$

$$Re_{e,Local} = \frac{d_e}{\mu_e}\left(\rho_{s,e}V_e\right)_{Local} = \frac{d_e}{\mu_e}C_{d,e}\sqrt{2\rho_{s,e}\Delta P_{e,Local}} \tag{19}$$

$$M_{e,Local} = \frac{V_{e,Local}}{\sqrt{\gamma R T_{s,e}}} = \frac{C_{d,e}\sqrt{2\Delta P_{e,Local}}}{\sqrt{\rho_{s,e}}\sqrt{\gamma R T_{s,e}}} \tag{20}$$

Here, the local main flow channel dynamic pressure ($\Delta P_{e,Local}$) is the difference between the local mainstream flow stagnation pressure and the local mainstream flow static pressure.

2.6 Measurement of surface heat transfer coefficient and adiabatic wall temperature distributions – mainstream side of effusion plate

For the mainstream flow side of the effusion plate, a transient approach is utilized to measure spatially-resolved distributions of adiabatic surface temperature (which is used to determine adiabatic film cooling effectiveness), and heat transfer coefficients. Figure 4 shows the experimental arrangement. Additional details are provided by Ligrani et al. [1].

To obtain the present data, the infrared radiation emitted by the film cooled interior surface of the channel is captured using a FLIR Systems Inc. ThermoVision® T650sc Infrared Camera (S/N 22700776), which operates at infrared wavelengths from 7.5 μm to 13.0 μm. This camera is operated with a FLIR T197915 45 degree infrared lens. Temperatures, measured using the calibrated, copper-constantan (Type-T) thermocouples distributed along the test surface adjacent to the flow, are used to perform the *in situ* calibrations simultaneously as the radiation contours from

surface temperature variations are recorded. The resulting calibration data are used to convert gray scale infrared image data to local temperature distributions.

This is accomplished as the camera views the polystyrene test surface through a zinc-selenide window located in the top wall of the experimental facility shown in Fig. 4. Within this figure, the infrared camera is located within an area adjacent to the mainstream flow, but on the opposite side of the test section relative to the film cooled surface. Because of its low thermal conductivity (of approximately 0.22 W/mK), the polystryrene surface provides a near-adiabatic surface boundary condition. In general, two to five thermocouple junction locations are present in the infrared field viewed by the camera. The exact spatial locations and pixel locations of these thermocouple junctions and the coordinates of the field of view are known from calibration maps obtained prior to measurements. During this procedure, the camera is focused, and rigidly mounted and oriented relative to the test surface in the same way as when radiation contours are recorded. Voltages from the thermocouples are acquired using the apparatus mentioned earlier. With these data, gray scale values at pixel locations within digital images from the infrared imaging camera are readily converted to local surface temperature values. Because such calibration data depend strongly on camera adjustment, the same brightness, contrast, and aperture camera settings are used to obtain the experimental data. The *in situ* calibration approach rigorously and accurately accounts for these variations (see Appendix D).

When obtaining data, a sequence of digital images is captured from the infrared camera at a rate of 5 Hz. Each digital image from the infrared camera represents an array of wall temperatures at varying x and y locations for a given time t which is equal to the frame number multiplied by the sampling frequency. The images are recorded using FLIR ResearchIR software, and are exported as a grayscale video in *.wmv format. The time-sequence of digital images is loaded into a MATLAB script which converts each pixel of each frame into a grayscale value from 0 to 255. These images are then in the form of gray scale bit maps. These images are then imported into MATLAB software to convert each of 256 possible gray scale values to local surface temperature at each pixel location using calibration data. Each individual image covers a 640 pixel by 480 pixel area, with each pixel representing a 0.14 mm^2 area of the test surface.

The present work focuses on providing local and line-averaged adiabatic wall temperatures, adiabatic film cooling effectiveness, and heat transfer coefficients for a range of blowing ratios. These data are produced using the impulse response method described by Oldfield

[22]. The impulse response technique was originally developed to process signals from thin-film heat transfer gauges [23] and was first used by Anthony et al. [24]. It was later used in conjunction with infrared thermography to measure heat transfer characteristics on turbine blade tips by O'Dowd et al. [23]. It is a computationally efficient method to reconstruct heat flux from discrete temperature samples taken at some sampling frequency. It uses known pairs of exact solutions to generate an impulse response digital filter, which is used with MATLAB filter routines to convert temperature into heat flux using a Fast Fourier Transform. According to O'Dowd et al. [23], this process is more sophisticated than earlier techniques employed for heat flux reconstruction.
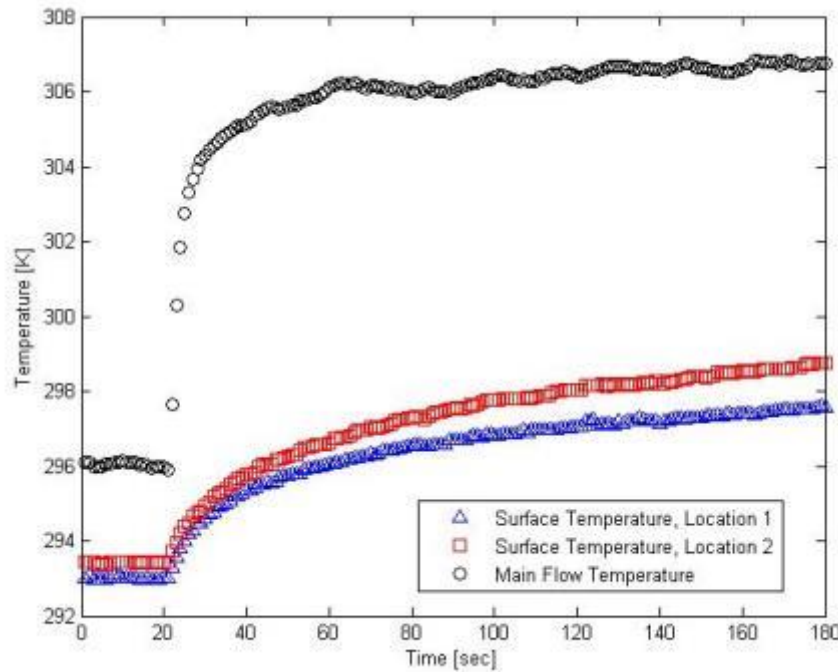
Figure 13. Example of temperature variations with time of the main flow and two points on the test surface during a typical transient test.
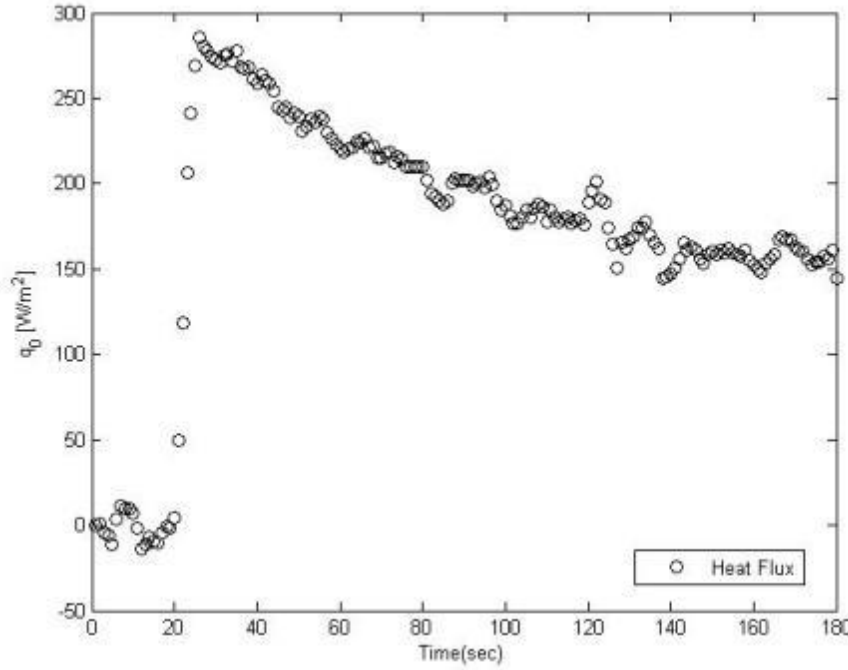
Figure 14. Example of heat flux variations with time at a single point on the test surface during a typical transient test.

To account for any surface temperature variations at the beginning of a test, including local deviations from an adiabatic condition, a complete heat flux history for each surface location is reconstructed from temperature traces which are measured and provided by the infrared camera. Infrared imaging is thus employed here to obtain transient surface temperature data, which is utilized to reconstruct heat transfer data (Figs. 13 and 14). As such, the approach requires the use of two heater meshes to provide a near-instantaneous step-change in mainstream temperature, and an infrared camera to measure time-varying and spatially-resolved distributions of surface temperature. At each time step, the associated value for heat flux is the average of five heat flux data points taken at different times. With the present configuration, a freestream static temperature increase of 11-12°C is obtained with V_m=4.94-5.10 m/s, a temperature increase of 8.0-8.5°C is obtained with V_m=7.02-7.18 m/s, and a temperature increase of 7.0-7.5°C is obtained with V_m=9.08-9.22 m/s.

According to O'Dowd et al. [23], the associated equations are comprised of Fourier's law of heat conduction for a one-dimensional, unsteady, semi-infinite solid (Eqn. (21)) which is solved

using an initial condition (Eqn. (22)) and two boundary conditions (Eqns. (23) and (24)). These equations are given as follows

$$k \frac{\partial^2 T}{\partial z^2} = \rho c \frac{\partial T}{\partial t} \tag{21}$$

$$T(z, t = 0) = T_i \tag{22}$$

$$T(z = \infty, t) = T_i \tag{23}$$

$$k \frac{\partial T}{\partial z}\bigg|_{z=0} = h_C(T_{aw} - T_{surf}) \tag{24}$$

The initial condition assumes that the initial temperature for any part of the solid is a constant T_i. The first boundary condition assumes that for a semi-infinite solid, the temperature at the maximum depth of the solid is unaffected by the thermal load at the surface and maintains the initial temperature, T_i for the entire test. The second boundary condition is a convective boundary condition and is imposed by sudden transient heating. The solution to Eqn. (21) with the given initial and boundary conditions is then given by

$$\frac{T_w(t) - T_i}{T_\infty - T_i} = 1 - erf\left(\frac{z}{2\sqrt{\alpha t}}\right) - \left[\exp\left(\frac{h_c z}{k} + \frac{h_c^2 \alpha t}{k^2}\right)\right] \times \left[1 - erf\left(\frac{z}{2\sqrt{\alpha t}} + \frac{h_c \sqrt{\alpha t}}{k}\right)\right] \tag{25}$$

The solution to this equation is a function of the initial temperature, the wall temperature (as a function of time), the mainstream temperature, the thermal characteristics of the solid, including the depth of the solid, the Biot number ($\frac{h z}{k}$), and the convective heat transfer coefficient, h.
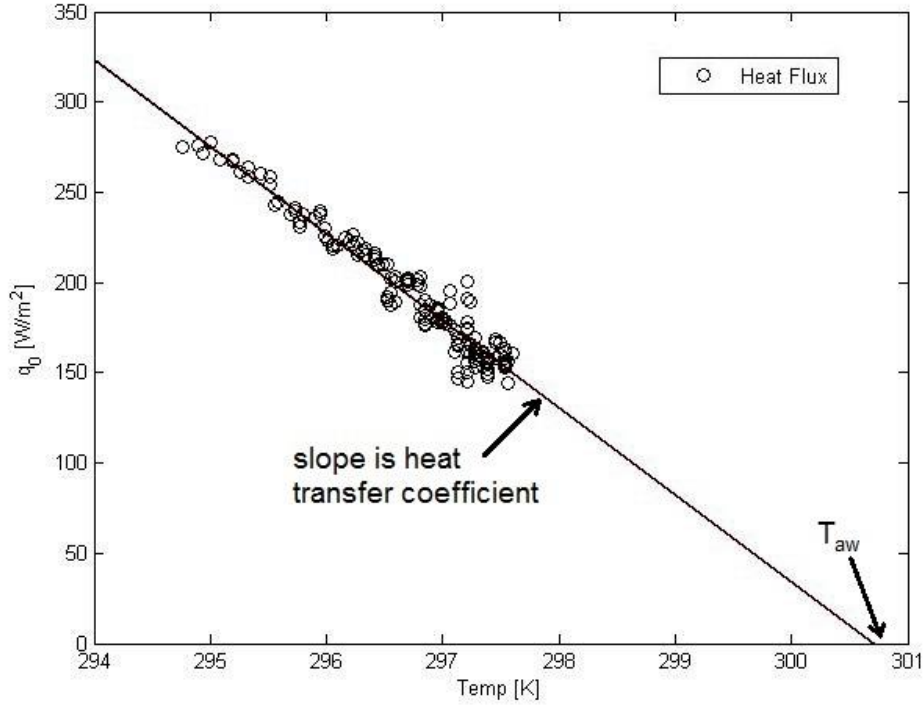
Figure 15. Example of variation of local surface heat flux with surface temperature for one test surface location during a typical transient test.

After reconstruction of the heat flux from temperature traces, the heat flux is then plotted against temperature for the time period over which the heater mesh is operating. A linear relationship between the heat flux and wall temperature is expected and observed when using the linear convective heat transfer equation. An example from the present investigation is shown in Fig. 15. Within this figure, the slope has the magnitude of the heat transfer coefficient and adiabatic wall temperature is extrapolated for zero surface heat flux. In order to accommodate for small fluctuations in the mainstream flow, a non-dimensional approach is used, which also reduces uncertainty, and leads to results which are more repeatable.

Measured spatially-resolved distributions of adiabatic surface temperature are then used to determine local values of the spatially-resolved surface effectiveness, using the equation given by

$$\eta = (T_{aw} - T_{s,M})/(T_{t,C} - T_{s,M}) \tag{26}$$

The heat transfer coefficient is then defined by the equation given by

$$\dot{q_o}" = h(T_{aw} - T_{surf})$$ (27)

Line-averaged adiabatic wall temperature and heat transfer coefficient values are determined by averaging the quantity of interest for a row of pixels at constant x/d_e for a range of y/d_e. For the present study, this y/d_e range is from -4 to +4.

The temperature ratio is defined as the ratio of mainstream temperature to coolant temperature. The density ratio is defined as the ratio of mainstream density to coolant density. As temperature ratio increases, density ratio decreases for air.

2.7 Measurement of surface heat transfer coefficient and adiabatic wall temperature distributions – coolant side of effusion plate

Liquid crystal thermography is employed to acquire spatially-resolved surface temperature distributions on the coolant side of the effusion plate. This technique is currently under development for future tests. The present experiment uses only infrared data on the film cooled side of the test plate. Figure 4 shows the instrumentation arrangement. For the impingement cooled side of the effusion test plate, a thin etched-foil film heater is installed beneath a 1.5 mm thick layer of polystyrene (which is located next to the air stream) to provide a constant surface heat flux thermal boundary condition. This heater is custom designed and installed by Electrofilm Manufacturing Co. The exposed surface of the polystyrene is coated with micro-encapsulated liquid crystals produced by LCR HALLCREST LLC - US. Thermochromic liquid crystal images are captured and recorded using a JAI CB-040GE compact digital color progressive scan charge-coupled camera. The impingement hole plate is made of optically transparent acrylic to allow the CCD camera to observe the cooled test surface, as it is located within the impingement plenum. With this arrangement, specially-designed LED light strips are used to illuminate the thermochromic liquid crystal images for the CCD camera.

2.8 Experimental uncertainty magnitudes

Uncertainty estimates are based on 95 percent confidence levels, and determined using procedures described by Kline and McClintock [28] and by Moffat [29]. Uncertainty of

thermocouple temperature readings is ± 0.15 ºC. This uncertainty is dependent upon the thermocouple calibration procedure. Pressure uncertainty is ± 0.25 Pa. This uncertainty is dependent upon the pressure transducer calibration procedure. Spatial and temperature resolutions achieved with the infrared imaging are about 0.2 mm and $0.75\,^{\circ}$C, respectively. This spatial resolution corresponds to the distance associated with half-spacing between two adjacent pixels within a typical infrared image. This magnitude of temperature resolution is due to uncertainty in determining the exact locations of thermocouples with respect to pixel values used for the *in situ* calibrations. The experimental uncertainty of the blowing ratio is ± 4.0 percent. The experimental uncertainty of the coolant mass flow rate is also approximately ± 4.0 percent, and is primarily due to uncertainty in local coolant velocity. This local coolant velocity value is a result of uncertainty in measured coolant pressure ratio (± 0.8 percent) and uncertainty in the discharge coefficient (± 3.4 percent). Local surface effectiveness uncertainty is estimated to be ± 0.033 or about ± 8.2 percent for a nominal effectiveness value of 0.4. Experimental uncertainty magnitudes of line-averaged heat transfer coefficients are ± 8-10 percent, or approximately ± 4.5 W/m^{2}K for a spanwise-averaged heat transfer coefficient value of 50 W/m^{2}K. These estimates include the influences of radiation and conduction losses and heat transfer to and from the test surface.

CHAPTER 3

EXPERIMENTAL RESULTS

The effects of varying blowing ratio, varying main flow velocity, and varying main flow temperature on adiabatic wall temperature distributions, adiabatic film cooling effectiveness distributions, and heat transfer coefficient distributions are presented and described for a sparse effusion cooling hole array.

3.1 Local Data

Figures 16 through 24 present local, spatially-resolved adiabatic wall temperature, adiabatic film cooling effectiveness, and heat transfer coefficient data.
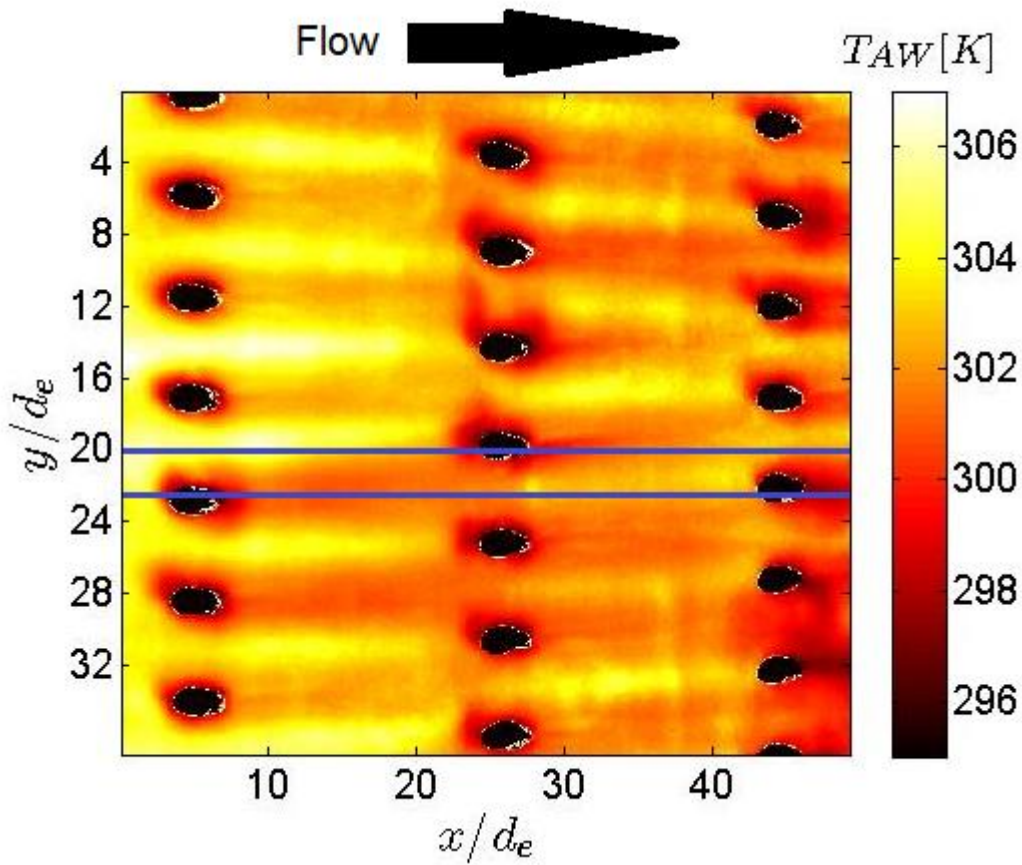
Figure 16. Local, spatially-resolved surface adiabatic wall temperature distribution with main flow velocity of 5 m/s, main flow temperature of 307 K, and blowing ratio of 4.09.

Figure 16 presents a surface distribution of adiabatic wall temperature in degrees Kelvin for a main flow velocity of 5 m/s and an average blowing ratio of 4.09. The data show that adiabatic wall temperature values are higher between and away from the holes and lower downstream of the film cooling holes. Lower values of adiabatic wall temperature indicate better protection of the surface from the hot main flow gas since the film cooling supply is at a lower temperature than the main flow. The data shows fairly good periodicity in each row of holes. The data shows a reduction in adiabatic wall temperature as x/d_e increases from 0 to 50. This is due to the increased concentrations and accumulations of film near to the surface, as the bulk flow advects downstream, and additional rows of holes are encountered. The streamwise location x/d_e=0 represents the leftmost plate location visible to the infrared camera. It occurs between the second and third rows of holes in the test plate.
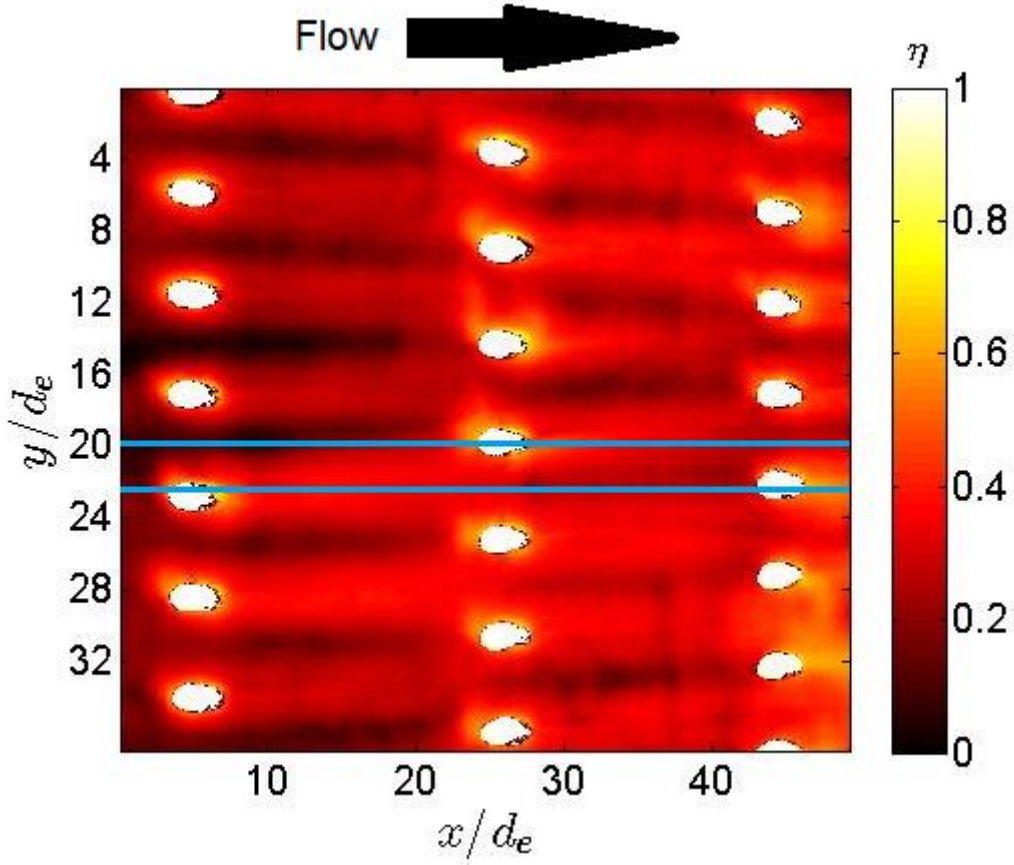
Figure 17. Local, spatially-resolved surface adiabatic film cooling effectiveness distribution with main flow velocity of 5 m/s, main flow temperature of 307 K, and blowing ratio of 4.09.

Figure 17 presents a surface distribution of dimensionless adiabatic film cooling effectiveness for a main flow velocity of 5 m/s and an average blowing ratio of 4.09. The data from Fig. 16 are used to obtain these adiabatic effectiveness data. However, for adiabatic effectiveness, higher values reflect larger concentrations of film on the surface, and better protection of the surface from the hot main flow gas. Similar to Fig. 16, the data show that adiabatic effectiveness values are lower between and away from the holes and higher downstream of the film cooling holes. Figure 17 also shows overall increases in adiabatic effectiveness as X/d_e increases from 0 to 50, due to increased accumulations of film near to the downstream parts of the test surface.
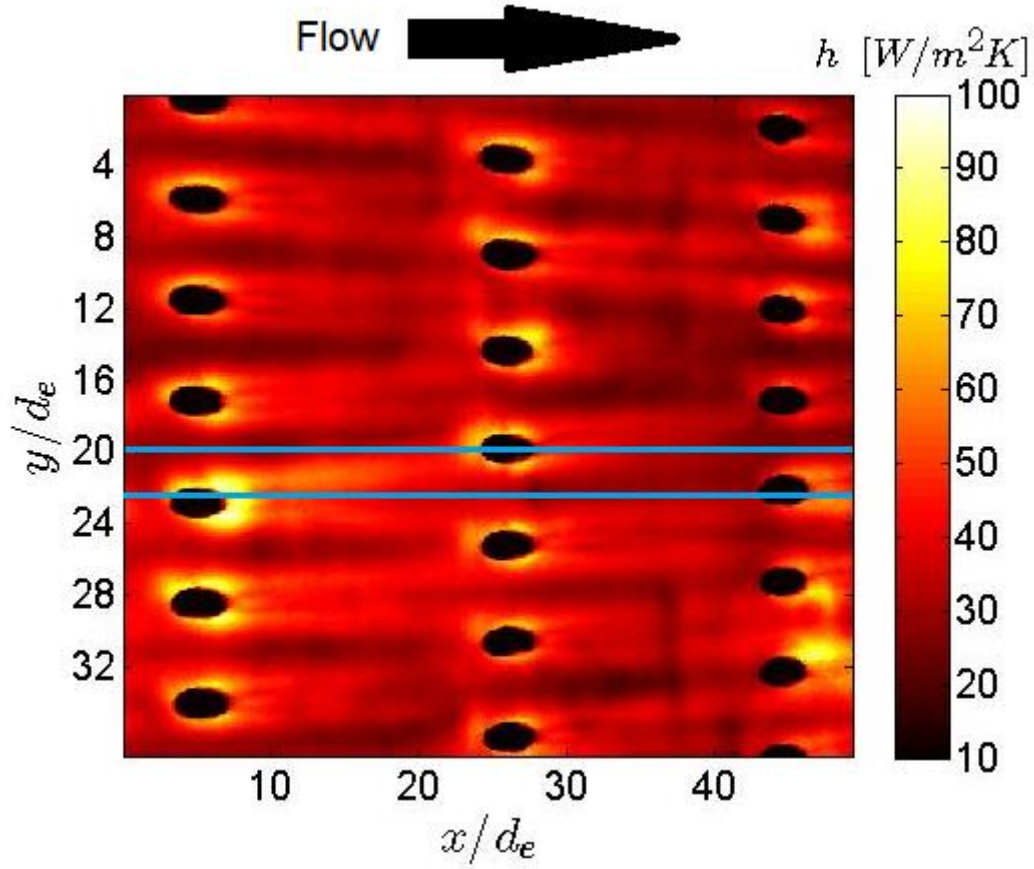
Figure 18. Local, spatially-resolved surface heat transfer coefficient distribution with main flow velocity of 5 m/s, main flow temperature of 307 K, and blowing ratio of 4.09.

Figure 18 presents a surface distribution of heat transfer coefficient in dimensional form [W/m²K] for a main flow velocity of 5 m/s and an average blowing ratio of 4.09. Here, heat transfer coefficients range from approximately 20 W/m²K to 90 W/m²K along the test surface. Higher heat transfer coefficient values are generally observed just upstream and around the holes. This is due to the horseshoe vortex that forms around the flow leaving an individual film cooling hole. Lower heat transfer coefficient values are observed away from the holes. Lower values of heat transfer coefficient indicate less mixing between the film cooling gas and the hot main flow gas, which leads to better protection of the surface from the hot main flow gas. The data shows fairly good spatial periodicity when compared for different hole locations. Higher values of heat transfer coefficient are generally observed at locations where local turbulent transport and local mixing are augmented.

Additional local data are shown in Figs. 19 through 24. These figures show streamwise data variations for locations of $Y/d_e=20$ and $Y/d_e=23$. Note that the data shows excellent spanwise periodicity and uniformity. Such behavior evidences flow characteristics which are spanwise uniform at the entrance to the test section.
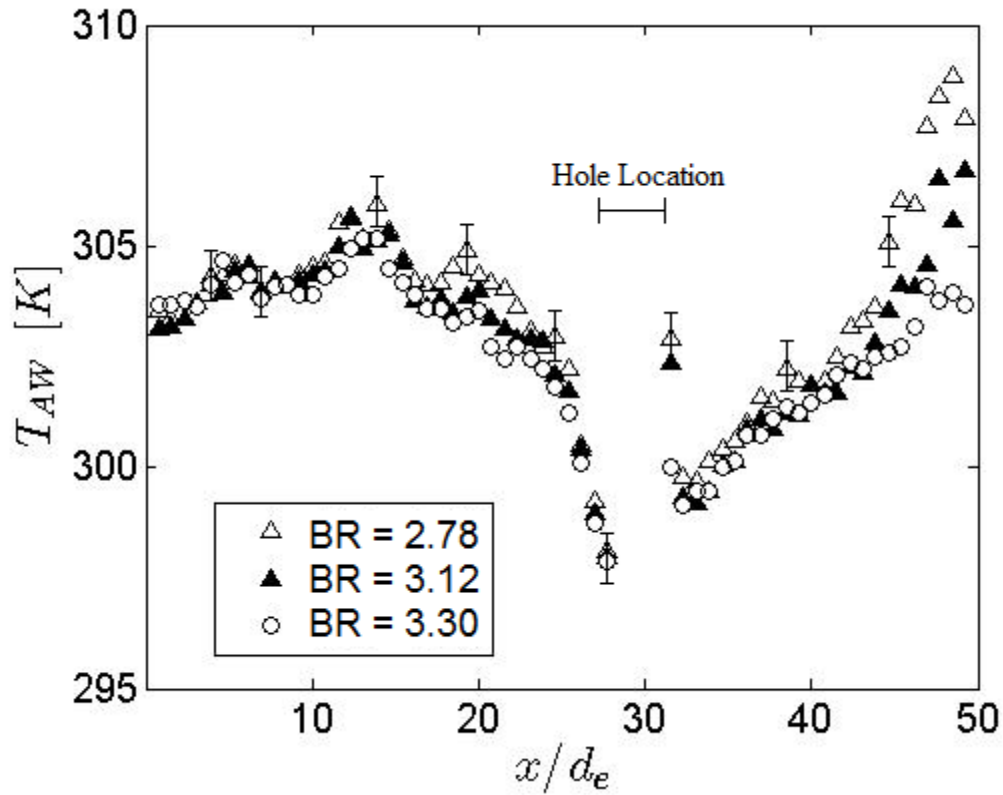
Figure 19. Streamwise variation of local, spatially-resolved adiabatic wall temperature at location $Y/d_e = 20$ with main flow velocity of 9 m/s, main flow temperature of 304 K, and blowing ratios of 2.78, 3.12, and 3.30 including error bars.
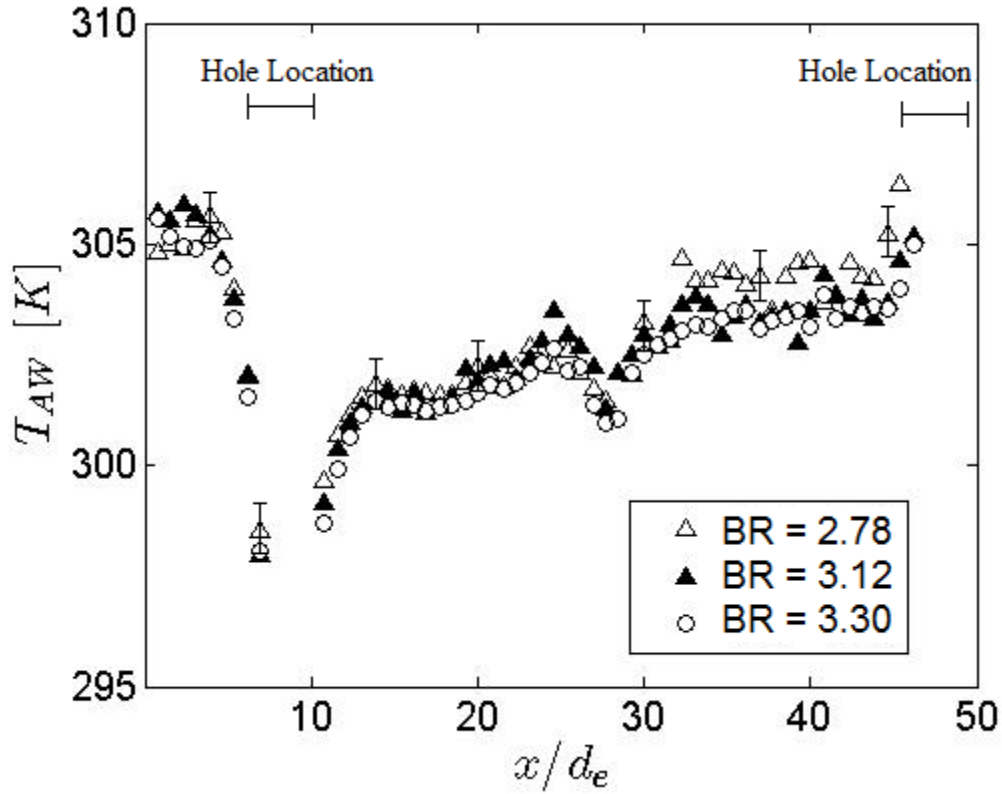
Figure 20. Streamwise variation of local, spatially-resolved adiabatic wall temperature at location $Y/d_e = 23$ with main flow velocity of 9 m/s, main flow temperature of 304 K, and blowing ratios of 2.78, 3.12, and 3.30 including error bars.

Figures 19 and 20 present local adiabatic wall temperature data, in Kelvin, as a function of X/d_e for a main flow velocity of 9 m/s and average blowing ratios of 2.78, 3.12, and 3.30. These data are given for Y/d_e locations of 20 and 23. Here, adiabatic wall temperature values range from about 297 K to 309 K. In both locations, the adiabatic wall temperature generally decreases as the blowing ratio increases, when compared at a particular X/d_e location. As mentioned, blowing ratio is spatially-averaged over the test surface. Lower values of adiabatic wall temperature indicate higher concentration of film cooling air near the test surface, which gives better protection of the surface from the hot main flow gas.
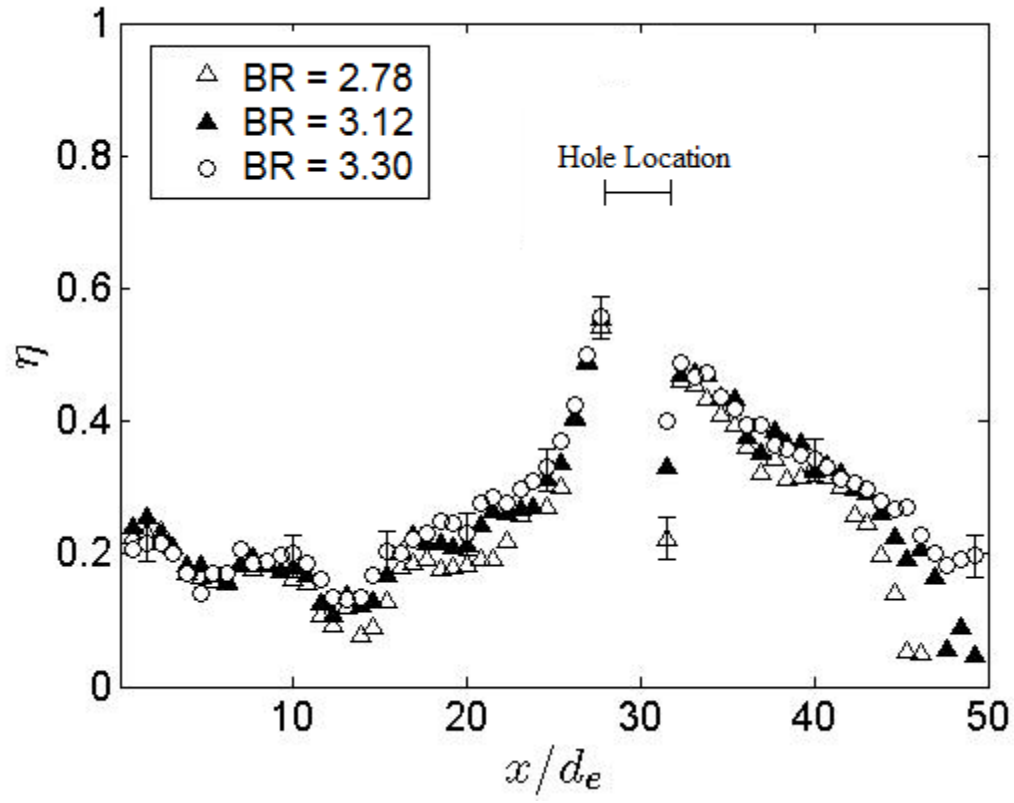
Figure 21. Streamwise variation of local, spatially-resolved adiabatic film cooling effectiveness at location $Y/d_e = 20$ with main flow velocity of 9 m/s, main flow temperature of 304 K, and blowing ratios of 2.78, 3.12, and 3.30 including error bars.
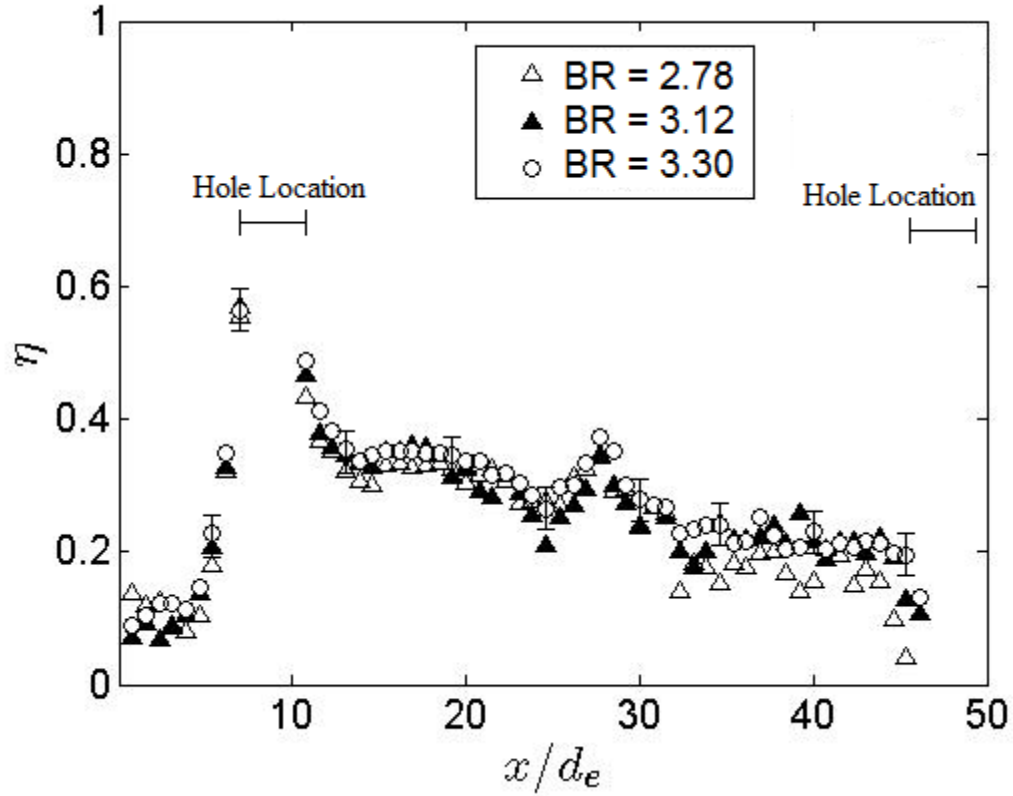
Figure 22. Streamwise variation of local, spatially-resolved adiabatic film cooling effectiveness at location $Y/d_e = 23$ with main flow velocity of 9 m/s, main flow temperature of 304 K, and blowing ratios of 2.78, 3.12, and 3.30 including error bars.

Figures 21 and 22 present local adiabatic film cooling effectiveness data as a function of X/d_e for a main flow velocity of 9 m/s and average blowing ratios of 2.78, 3.12, and 3.30 at locations of Y/d_e=20 and Y/d_e=23. The data from Figs. 19 and 20 are used to obtain these adiabatic effectiveness data. Here, higher values of adiabatic effectiveness reflect larger concentrations of film near the test surface, and better protection of the surface from the hot main flow gas. Consistent with results in Figs. 19 and 20, local adiabatic effectiveness generally increases as the blowing ratio increases.
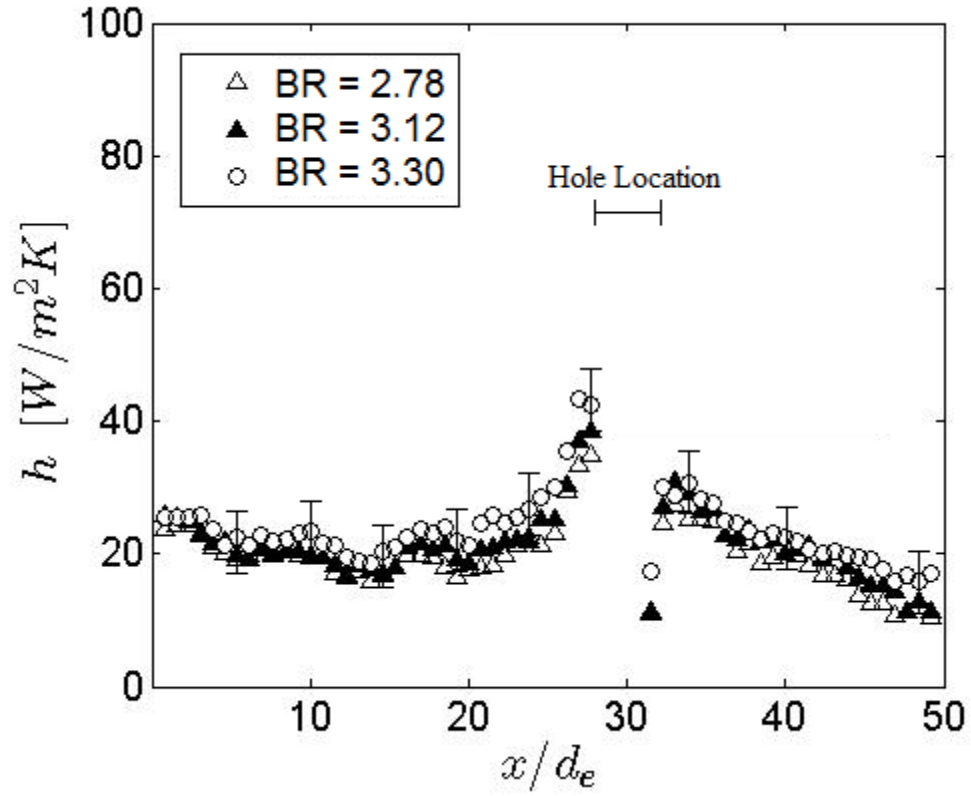
Figure 23. Streamwise variation of local, spatially-resolved heat transfer coefficient at location Y/d_e = 20 with main flow velocity of 9 m/s, main flow temperature of 304 K, and blowing ratios of 2.78, 3.12, and 3.30 including error bars.
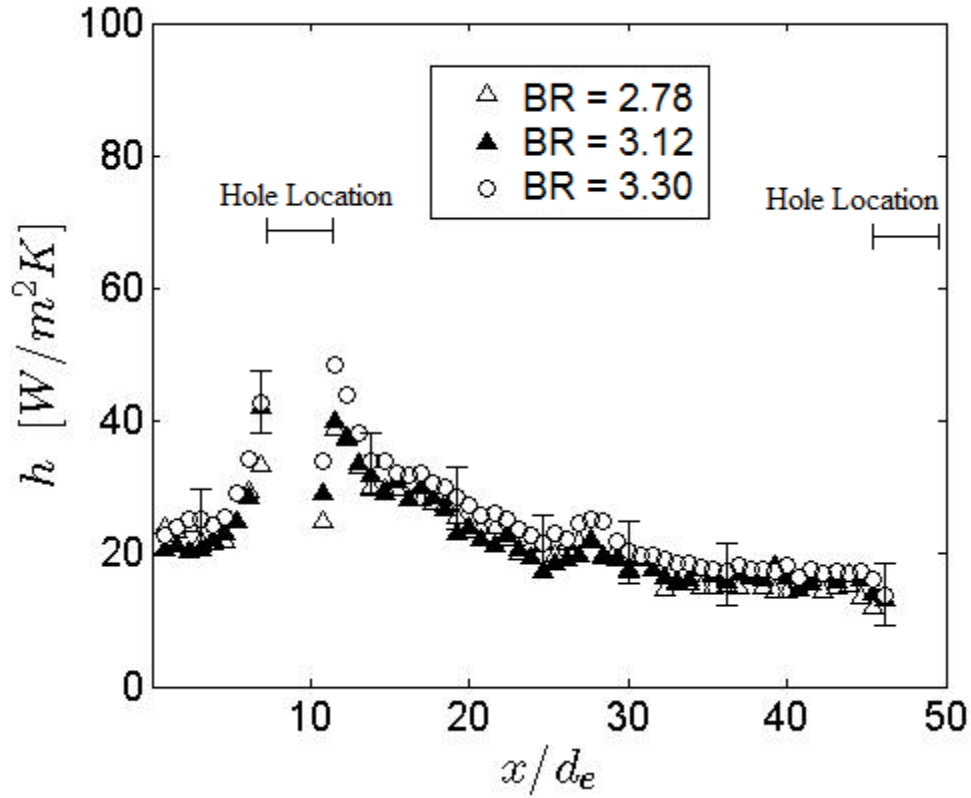
Figure 24. Streamwise variation of local, spatially-resolved heat transfer coefficient at location $Y/d_e = 23$ with main flow velocity of 9 m/s, main flow temperature of 304 K, and blowing ratios of 2.78, 3.12, and 3.30 including error bars.

Figures 23 and 24 present local heat transfer coefficient data in dimensional form [W/m²K], as a function of X/d_e for a main flow velocity of 9 m/s and average blowing ratios of 2.78, 3.12, and 3.30. These data are given for Y/d_e locations of 20 and 23. Here, heat transfer coefficient values range from about 10 W/m²K to 50 W/m²K. The heat transfer coefficient does not show much variation with blowing ratio, but generally the data increase as the blowing ratio increases. Lower values of heat transfer coefficient indicate less mixing between the film cooling gas and the hot main flow gas, which leads to better protection of the surface from the hot main flow gas. The slight increase observed with increased blowing ratio is due to increased three-dimensional turbulent transport, increased mixing, increased three-dimensional turbulent diffusion. Higher values in the immediate vicinity of the holes are consistent with this observation. Note that no data are given for the hole locations.

3.2 Line-Averaged Data

Figures 25 through 32 present line-averaged adiabatic wall temperature, adiabatic film cooling effectiveness, and heat transfer coefficient data. These averages are determined without including contributions at film cooling hole locations.
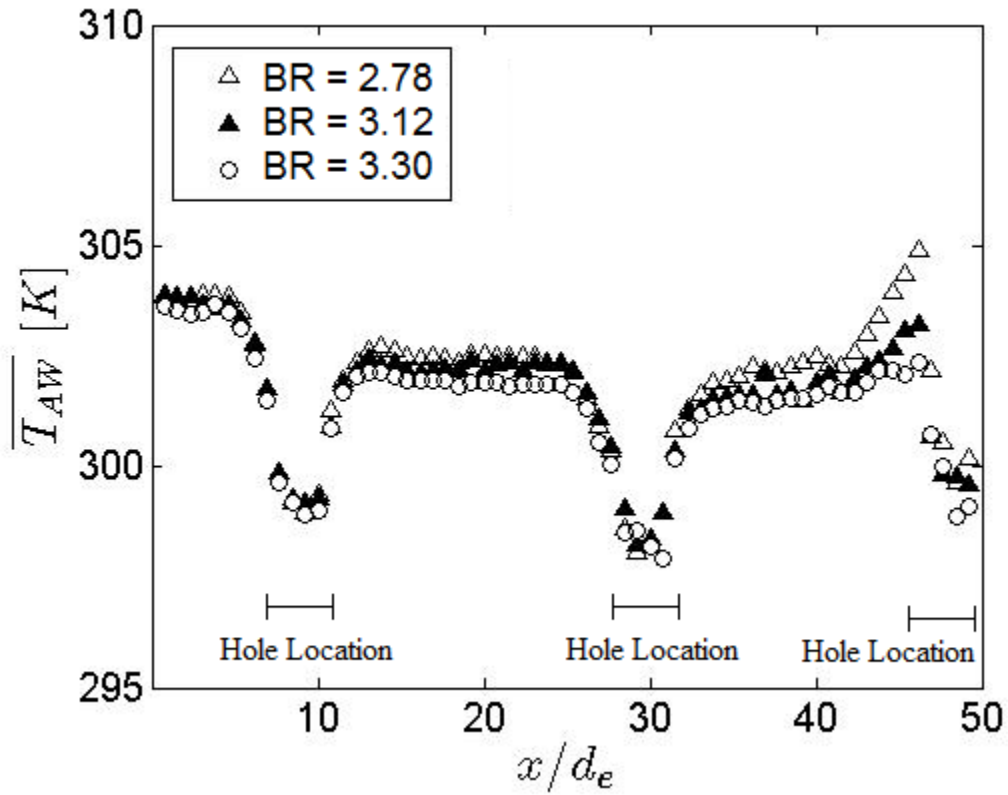
Figure 25. Streamwise variation of line-averaged adiabatic wall temperature with main flow velocity of 9 m/s, main flow temperature of 304 K, and blowing ratios of 2.78, 3.12, and 3.30.
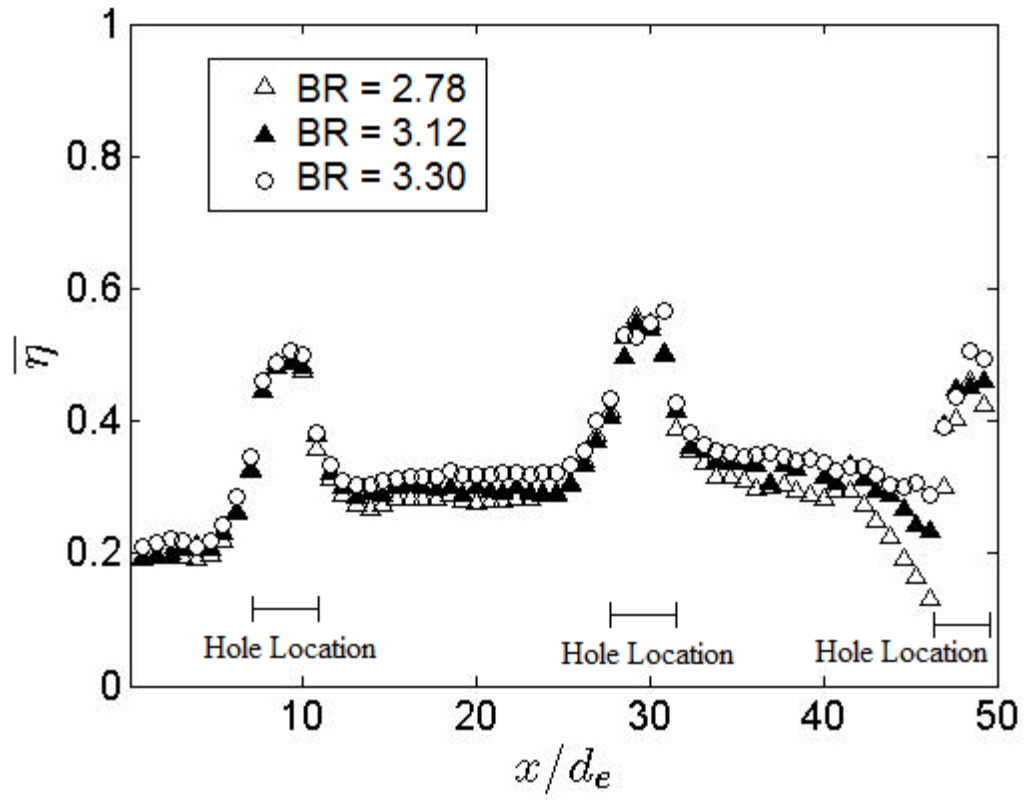
Figure 26. Streamwise variation of line-averaged adiabatic film cooling effectiveness with main flow velocity of 9 m/s, main flow temperature of 304 K, and blowing ratios of 2.78, 3.12, and 3.30.
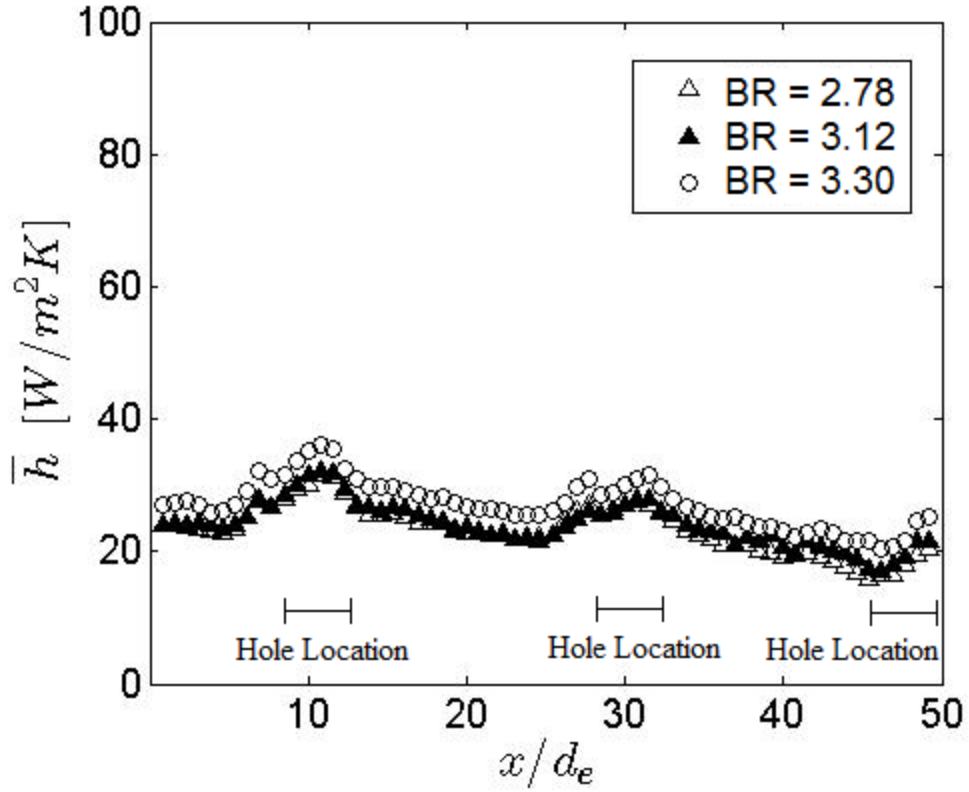
Figure 27. Streamwise variation of line-averaged heat transfer coefficient with main flow velocity of 9 m/s, main flow temperature of 304 K, and blowing ratios of 2.78, 3.12, and 3.30.

Figures 25, 26, and 27 present line-averaged adiabatic wall temperature, line-averaged adiabatic film cooling effectiveness, and line-averaged heat transfer coefficient data, respectively, as a function of X/d_e for a main flow velocity of about 9 m/s and average blowing ratios of 2.78, 3.12, and 3.30. The data in Fig. 25 show that line-averaged adiabatic wall temperature generally decreases as blowing ratio increases, as observed for local data, indicating that surface protection is improved as film concentration increases near the surface. Consistent trends are observed for the line-averaged adiabatic film cooling effectiveness distribution in Fig. 26. The data in Fig. 27 show that line-averaged heat transfer coefficient values generally increase as the blowing ratio increases, as observed for local data. This decrease in surface protection is believed to be due to film cooling jets lift-off phenomena, and increased local mixing near film cooling concentrations.
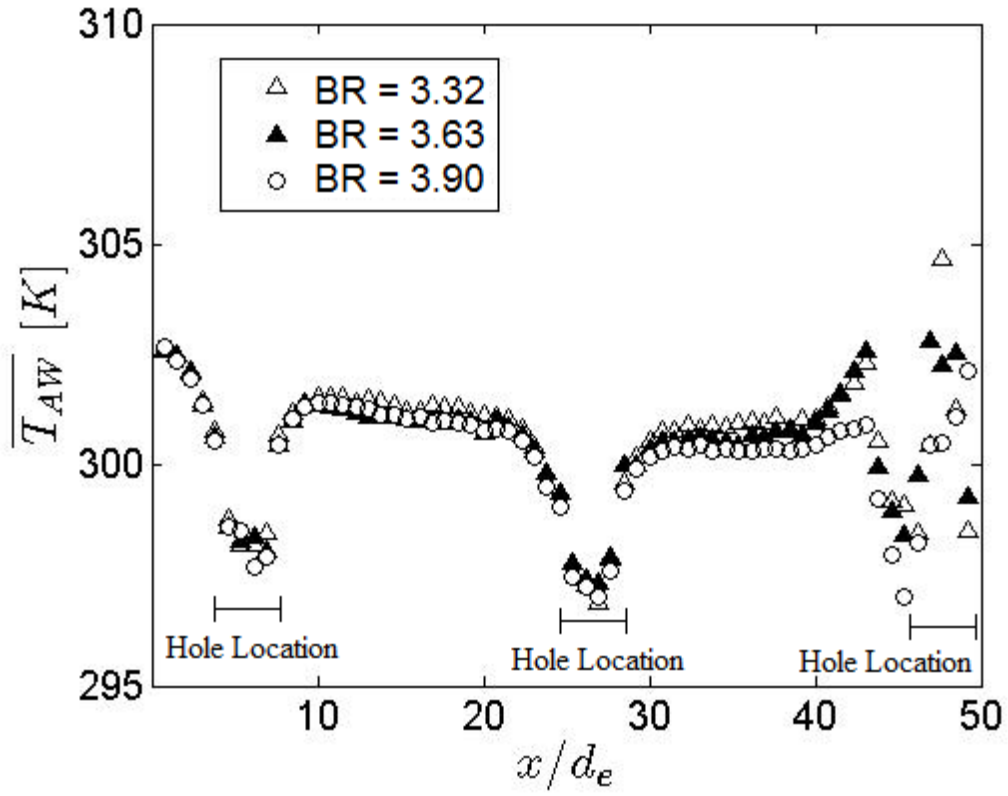
Figure 28. Streamwise variation of line-averaged adiabatic wall temperature with main flow velocity of 7 m/s, main flow temperature of 304 K, and blowing ratios of 3.32, 3.63, and 3.90.
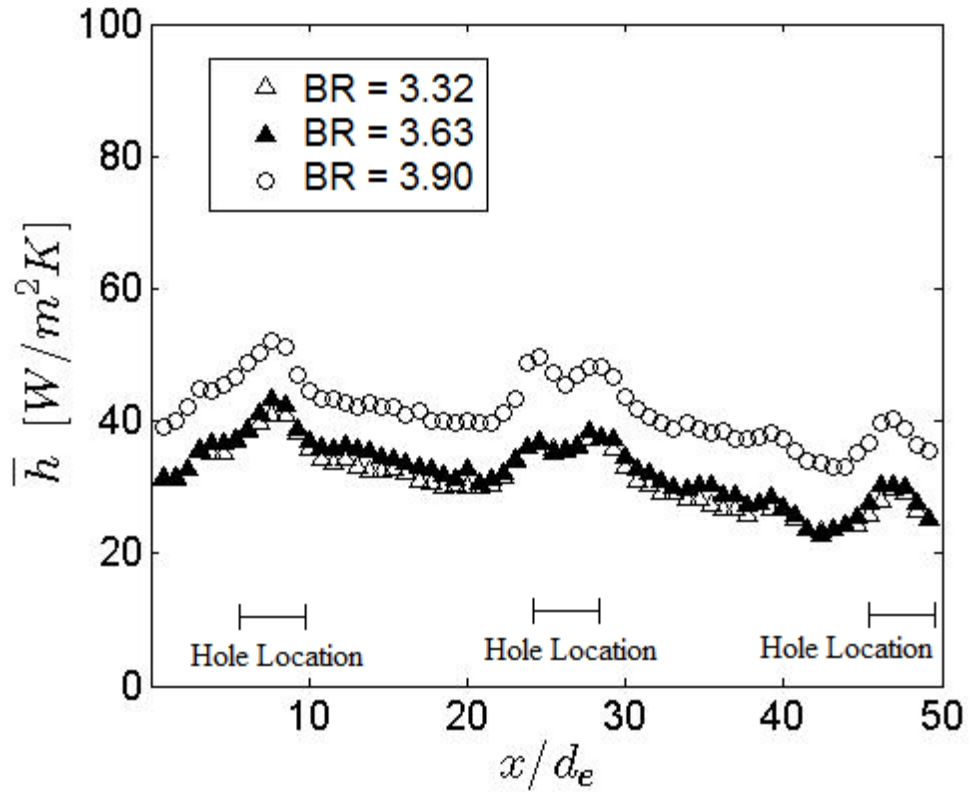
Figure 29. Streamwise variation of line-averaged heat transfer coefficient with main flow velocity of 7 m/s, main flow temperature of 304 K, and blowing ratios of 3.32, 3.63, and 3.90.

Figures 28 and 29 present line-averaged adiabatic wall temperature and line-averaged heat transfer coefficient data, respectively, as a function of X/d_e for a main flow velocity of 7 m/s and average blowing ratios of 3.32, 3.63, and 3.90. The trends observed in these figures are consistent with the trends observed in the data from Figs. 25 through 27, which are given for a higher main flow velocity.
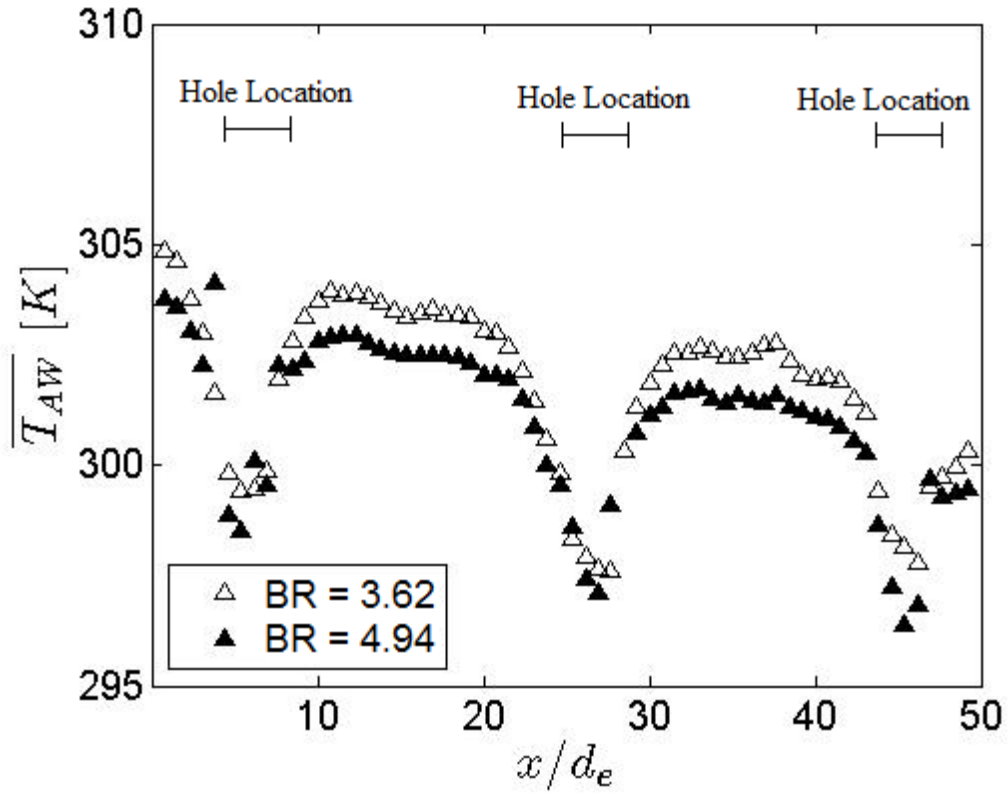
Figure 30. Streamwise variation of line-averaged adiabatic wall temperature with main flow velocity of 5 m/s, main flow temperature of 307 K, and blowing ratios of 3.62 and 4.94.
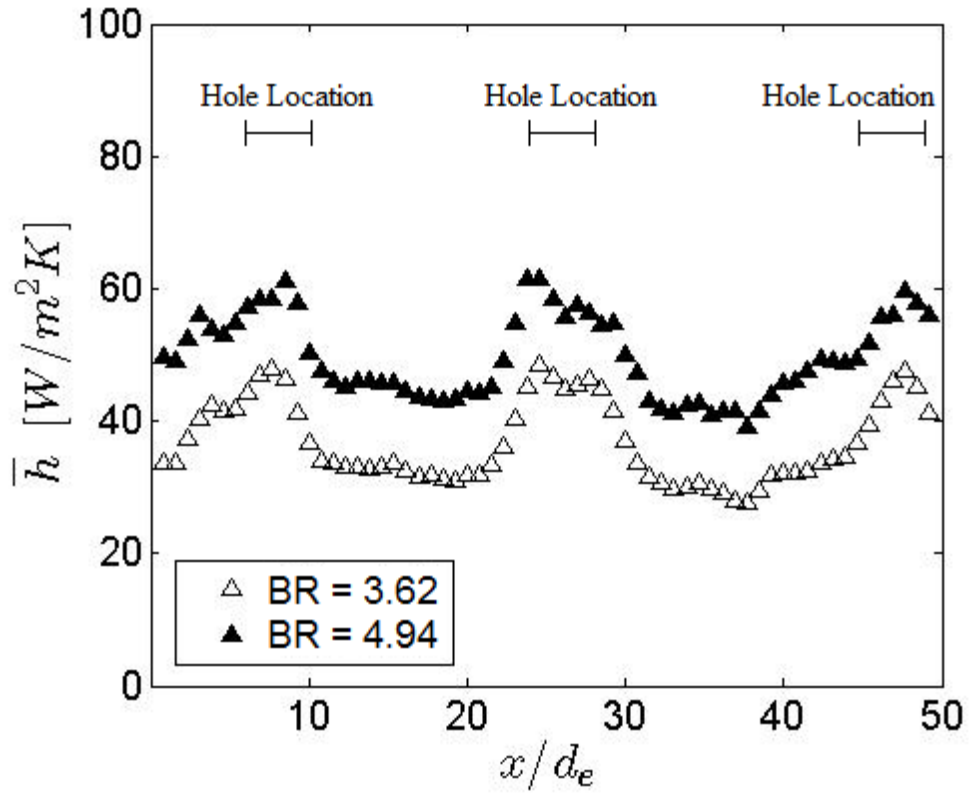
Figure 31. Streamwise variation of line-averaged heat transfer coefficient with main flow velocity of 5 m/s, main flow temperature of 307 K, and blowing ratios of 3.62 and 4.94.

Figures 30 and 31 present line-averaged adiabatic wall temperature and line-averaged heat transfer coefficient data, respectively, as a function of X/d_e for a main flow velocity of 5 m/s and average blowing ratios of 3.62 and 4.94. From these data, it is apparent that line-averaged adiabatic wall temperature generally decreases with blowing ratio, and that line-averaged heat transfer coefficient generally increases with blowing ratio.
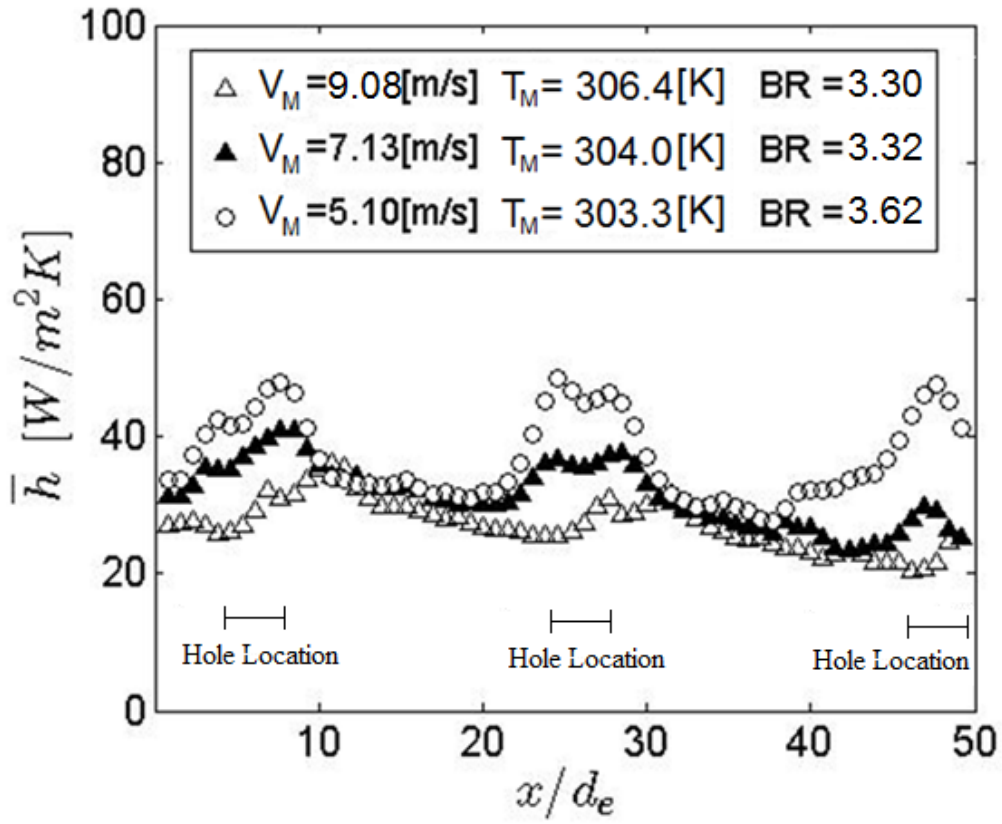
Figure 32. Streamwise variation of line-averaged heat transfer coefficient with main flow velocities of 5 m/s, 7 m/s, and 9 m/s; main flow temperatures of 307 K, 304 K, and 304 K; and blowing ratios of 3.62, 3.32, and 3.30.

Figure 32 presents a comparison of the heat transfer coefficient data at different freestream velocities. For this comparison, the blowing ratio is approximately the same for all cases, with values of 3.62, 3.32, and 3.30. The freestream temperature also changes for these different data sets, with a value of about 307 K for a main flow velocity of approximately 5.1 m/s, a value of about 305 K for a main flow velocity of approximately 7.1 m/s, and a value of 304 K for a main flow velocity of approximately 9.1 m/s. Though the blowing ratios are approximately the same, the advection speeds are changing as the main flow velocity increases. These data show that heat transfer coefficient decreases with increasing main flow velocity, particularly between and near the film cooling holes. This is due to a reduction in coolant lift-off of the film from the surface as coolant momentum decreases, and to lower freestream temperatures as mainstream speed increases.

	Main Flow		Cross Flow		Blowing Ratio
Exp#	V_M	$T_{s,M}$	V_C	$T_{s,M}$	BR
	[m/s]	[K]	[m/s]	[K]	[ ]
1	5.10	307	0.86	292	3.62
2	5.00	308	1.06	292	4.37
3	5.04	307	0.99	291	4.09
4	4.94	307	1.18	292	4.94
5	7.18	305	1.07	291	3.06
6	7.13	304	1.15	292	3.32
7	7.08	305	1.26	292	3.63
8	7.02	304	1.34	292	3.90
9	9.22	304	1.26	292	2.78
10	9.18	304	1.33	292	2.96
11	9.13	304	1.39	293	3.12
12	9.08	304	1.46	293	3.30

Table 1. Experimental conditions for each test case.

Table 1 presents the experimental conditions for the present study. Experiments 1 through 4 provide information on the effects of different blowing ratios for a main flow speed of about 5 m/s. Experiments 5 through 8 provide information on the effects of different blowing ratios for a main flow speed of about 7 m/s. Experiments 9 through 12 provide information on the effects of different blowing ratios for a main flow speed of about 9 m/s.

CHAPTER 4

SUMMARY AND CONCLUSIONS

Presented are full-coverage film cooling experimental data, for a film which develops along one surface of a double wall cooling test configuration. The new experimental facility used in these experiments is designed to impose flow conditions which simulate those which exist within combustor liner components of gas turbine engines. Measured quantities include surface variations of adiabatic wall temperature, adiabatic film cooling effectiveness, and heat transfer coefficient. The present experiment primarily deals with cross flow supplied full coverage film cooling for a sparse film cooling hole array that has not been previously tested. Data are provided for turbulent film cooling, a contraction ratio of 1, blowing ratios ranging from 2.78 to 4.94, coolant Reynolds numbers based on film cooling hole diameter of approximately 7,000 to 12,000, and mainstream temperatures from 304 K to 308 K. The film cooling hole array consists of a film cooling hole diameter of 6.4 mm with non-dimensional streamwise (X/d_e) and spanwise (Y/d_e) film cooling hole spacings of 15 and 4, respectively. The film cooling holes are streamwise inclined at an angle of 25 degrees with respect to the test plate surface and have adjacent streamwise rows staggered with respect to each other. Of particular interest are the effects of streamwise development, main flow velocity, and blowing ratio for a full-coverage film cooling array with a sparse hole spacing.

For the present experiments, adiabatic wall temperature values generally decrease with streamwise development, and adiabatic film cooling effectiveness values correspondingly increase with streamwise development. This is due to the increased concentrations of the film downstream of the holes and across the surface, as film accumulates, and additional rows of holes are encountered. Lower values of adiabatic wall temperature and higher values of adiabatic film cooling effectiveness indicate better thermal protection of the surface from the hot main flow gas. The data also show that heat transfer coefficient values generally increase with streamwise development and near holes. Such variations are due to the horseshoe vortex that forms around the flow leaving each film hole. At other locations, increased mixing between flows from successive rows of holes is responsible. Higher values of heat transfer coefficient indicate increased mixing between the film cooling gas and the hot main flow gas, which generally leads to reduced thermal protection of the test surface. The local values for adiabatic wall temperature, adiabatic film

cooling effectiveness, and heat transfer coefficient also show evidence of 3-dimensional conduction and conjugate heat transfer effects.

Experimental data from the present investigation also show that adiabatic wall temperature values generally decrease with increasing blowing ratio, and that corresponding adiabatic film cooling effectiveness values increase, provided comparisons are made at the same streamwise location and freestream velocity. The data also show that the heat transfer coefficient generally increases with increasing blowing ratio, where blowing ratio is a value which is spatially-averaged over the test surface. The decrease in adiabatic wall temperature and corresponding increase in adiabatic effectiveness are generally due to increased concentrations of film coolant near the test surface as blowing ratio increases. The slight increase in heat transfer coefficient observed with increased blowing ratio, especially in the immediate vicinity of the holes, is generally due to increased three-dimensional turbulent transport, increased mixing, and increased three-dimensional turbulent diffusion. Overall, for the range of blowing ratios considered, near-wall coolant concentrations generally increase with blowing ratio, which improves thermal protection, whereas local turbulent transport and mixing also increase with blowing ratio, which generally produces an opposite trend, of reduced surface thermal protection.

Near the film cooling holes, heat transfer coefficient values generally decrease with increasing mainstream flow velocity, provided comparisons are made for the same blowing ratio and same streamwise location. This is believed to be due to a reduction in coolant lift-off of the film from the surface as coolant momentum decreases, and to lower freestream temperatures as mainstream speed increases.

In conclusion, new data are presented which illustrate the capabilities of this new test facility, and illustrate the performance of a sparse effusion hole array. The facility uses three independent flow channels to provide double wall cooling arrangements which model the same configurations from operating gas turbine engines. The facility is designed to provide full coverage film cooling data and impingement cooling effectiveness data, wherein the film cooling flow is supplied using either cross flow, impingement flow, or a combination of both together. Within the present paper, data are given for the film cooled surface (or hot side) of the effusion test plate, with a cross flow supply for the film cooling air. The resulting data are useful for design of gas turbine components, as well as for the development and validation of codes for numerical prediction of such component flows. The channel and effusion cooling arrangement, including the sparse hole

47

arrangement, and associated experimental conditions are new, and as such, are different from any previous investigation.

APPENDIX A

EXPERIMENTAL TEST FACILITY: RANGE OF FLOW CONDITIONS

The flow conditions achieved using the double wall cooling experimental test facility now follow. The tests were conducted by varying the rotation rate of the main flow blower, the cross flow blower, and the impingement blower. Velocities in the main flow channel represent free stream velocities measured using a Kiel probe and a wall static pressure tap. Velocities in the cross flow channel represent spatially-averaged velocities, determined to be 80 percent of centerline velocities, also measured using a Kiel probe and a wall static pressure tap. Velocities in the impingement channel represent average velocities measured by the ASME orifice plate. The second page of values within the table below is a continuation of the first page of values. Included are discharge coefficient values. The determination of these discharge coefficients is based upon main flow free stream velocity, and cross flow channel spatially-averaged velocity.

| Test Reference | Main Flow Channel | | | Cross Flow Channel | | Impingement Channel | |
	Blower Setting [Hz]	Velocity [m/s]	Mass Flow Rate [kg/s]	Blower Setting [Hz]	Mass Flow Rate [kg/s]	Blower Setting [Hz]	Mass Flow Rate [kg/s]
9/14/2015 C1	20	3.8	0.47	0	0	20	0.045
9/14/2015 C2	30	5.8	0.73	0	0	20	0.045
9/14/2015 C3	40	7.8	0.98	0	0	20	0.046
9/14/2015 C4	50	9.7	1.22	0	0	20	0.046
9/14/2015 D1	40	8	1	0	0	10	0.024
9/14/2015 D2	40	7.9	0.99	0	0	15	0.035
9/14/2015 D3	40	7.9	0.99	0	0	20	0.046
9/14/2015 D4	40	7.7	0.96	0	0	25	0.057
10/01/2015 A1	21	4.1	0.52	10	0.030	0	0
10/01/2015 A2	21	4	0.5	15	0.042	0	0
10/01/2015 A3	21	3.9	0.49	20	0.055	0	0
10/01/2015 A4	21	3.8	0.47	25	0.069	0	0
10/02/2015 A1	21	4.1	0.52	10	0.028	0	0
10/02/2015 A2	21	4	0.5	15	0.041	0	0
10/02/2015 A3	21	3.9	0.49	20	0.054	0	0
10/02/2015 A4	21	3.8	0.48	25	0.068	0	0
10/05/2015 A1	21	4.1	0.51	10	0.029	0	0
10/05/2015 A2	21	4	0.5	15	0.041	0	0
10/05/2015 A3	21	3.9	0.49	20	0.054	0	0
10/05/2015 A4	21	3.8	0.47	25	0.067	0	0

	Impingement Plate				Effusion Plate				Blowing Ratio
	Velocity	Reynolds Number	Mach Number	Discharge Coefficient	Velocity	Reynolds Number	Mach Number	Discharge Coefficient	
Test Reference	[m/s]	[]	[]	[]	[m/s]	[]	[]	[]	[]
9/14/2015 C1	11.6	6110	0.033	0.42	20	8018	0.058	0.60	5.3
9/14/2015 C2	11.7	6169	0.034	0.42	20	8096	0.058	0.60	3.4
9/14/2015 C3	11.9	6263	0.034	0.42	21	8220	0.059	0.59	2.7
9/14/2015 C4	12.0	6331	0.035	0.42	21	8309	0.060	0.58	2.2
9/14/2015 D1	6.2	3294	0.018	0.41	11	4322	0.031	0.52	1.4
9/14/2015 D2	9.0	4764	0.026	0.42	15	6252	0.045	0.57	1.9
9/14/2015 D3	11.9	6311	0.034	0.42	21	8283	0.059	0.60	2.7
9/14/2015 D4	14.7	7805	0.042	0.42	25	10246	0.074	0.60	3.2
10/01/2015 A1	0	0	0	0	13	5383	0.039	0.72	3.3
10/01/2015 A2	0	0	0	0	19	7505	0.054	0.70	4.7
10/01/2015 A3	0	0	0	0	25	9917	0.072	0.71	6.3
10/01/2015 A4	0	0	0	0	31	12324	0.089	0.71	8.1
10/02/2015 A1	0	0	0	0	13	5130	0.037	0.68	3.1
10/02/2015 A2	0	0	0	0	18	7372	0.053	0.69	4.6
10/02/2015 A3	0	0	0	0	24	9791	0.071	0.70	6.3
10/02/2015 A4	0	0	0	0	31	12199	0.088	0.70	8.0
10/05/2015 A1	0	0	0	0	13	5295	0.038	0.70	3.2
10/05/2015 A2	0	0	0	0	18	7446	0.054	0.70	4.6
10/05/2015 A3	0	0	0	0	24	9651	0.070	0.69	6.2
10/05/2015 A4	0	0	0	0	30	12042	0.087	0.69	7.9

APPENDIX B

UNCERTAINTY ANALYSIS

Uncertainty analysis information is now presented. Uncertainty estimates are based on 95 percent confidence levels, and determined using procedures described by Kline and McClintock [28] and by Moffat [29]. Uncertainty of thermocouple temperature readings is $\pm 0.15\ ^{\circ}$C. This uncertainty is dependent upon the thermocouple calibration procedure. Pressure uncertainty is $\pm$ 0.25 Pa. This uncertainty is dependent upon the pressure transducer calibration procedure. Spatial and temperature resolutions achieved with the infrared imaging are about 0.2 mm and $0.75\ ^{\circ}$C, respectively. This spatial resolution corresponds to the distance associated with half-spacing between two adjacent pixels within a typical infrared image. This magnitude of temperature resolution is due to uncertainty in determining the exact locations of thermocouples with respect to pixel values used for the *in situ* calibrations. The experimental uncertainty of the blowing ratio is ± 4.0 percent. The experimental uncertainty of the coolant mass flow rate is also approximately ± 4.0 percent, and is primarily due to uncertainty in local coolant velocity. This local coolant velocity value is a result of uncertainty in measured coolant pressure ratio (± 0.8 percent) and uncertainty in the discharge coefficient (± 3.4 percent).

Heat flux data are calculated from transient infrared temperature samples using the impulse response method described by Oldfield [22]. The impulse response method is a computationally efficient method to reconstruct heat flux from discrete temperature samples taken at a known sampling frequency. At each time step, the associated value for heat flux is the average of five heat flux data points at different times. The transient heat flux data are used to determine a functional dependence of heat flux on temperature. The extrapolated temperature value based on this functional dependence for a value of zero heat flux is the adiabatic wall temperature. Based upon these considerations, the 95 percent confidence level uncertainty of adiabatic wall temperature is estimated to be $\pm 0.4\ ^{\circ}$C. Main flow recovery temperature and coolant stagnation temperature uncertainty is estimated to be $\pm 0.25\ ^{\circ}$C. Spatially-resolved distributions of adiabatic wall temperature are then used to determine local values of the spatially-resolved surface effectiveness, using the equation

$$\eta = (T_{aw} - T_{s,M})/(T_{t,C} - T_{s,M})$$

Local surface effectiveness uncertainty is estimated to be $\pm$ 0.033 or about $\pm$ 8.2 percent for a nominal effectiveness value of 0.4. Experimental uncertainty magnitudes of line-averaged heat transfer coefficients are $\pm$ 8-10 percent, or approximately $\pm$ 4.5 W/m^{2}K for a spanwise-averaged heat transfer coefficient value of 50 W/m^{2}K. These estimates include the influences of radiation and conduction losses and heat transfer to and from the test surface.

APPENDIX C

IN SITU INFRARED CALIBRATION

Additional discussion of the *in situ* method of infrared temperature measurement calibration is now presented. The infrared image collection system used was a FLIR Systems Inc. ThermoVision® T650sc Infrared Camera (S/N 22700776) with a FLIR T197915 45 degree infrared lens, which operates at infrared wavelengths from 7.5 μm to 13.0 μm. The infrared camera records radiation data over the test surface area as temperature varies with time. Calibrated, copper-constantan (Type-T) thermocouples, embedded in the test plate surface at known locations, record associated temperatures as they vary with time. The infrared camera records images of the test surface at a rate of 5 images per second. Each infrared camera image contains 307,200 pixels, distributed in a 640 pixel by 480 pixel array. At each pixel location over the test surface area, for each time step, the associated temperature measured by the infrared camera is converted to a grayscale value from 0 to 255 using MATLAB software. The temperature data recorded by the thermocouples are used to determine a functional dependence of temperature on grayscale value for the specific pixel locations where the thermocouples are located. The test surface is treated with a black coating, which reduces variations in emissivity across the test surface. The functional dependence of temperature on grayscale value determined for the thermocouple locations is applied to the entire test surface. Because calibration data depend strongly on brightness, contrast, aperture settings, camera position and relative angle to the test surface, test surface treatment, reflections, and ambient temperature, the *in situ* calibration approach rigorously and accurately accounts for variations between experiments. An example plot of the relationship between temperature and grayscale value follows.

Thermocouple Calibration

Slope = 0.0307, Intercept = 18.38
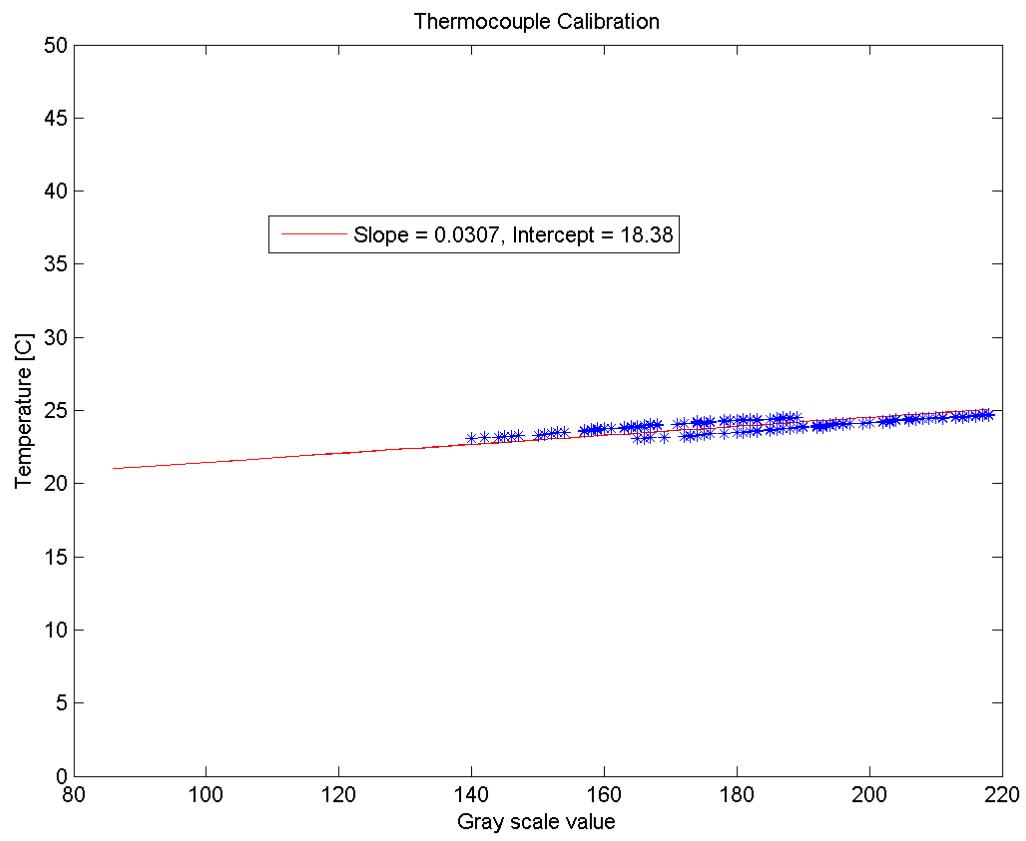
APPENDIX D

GROUND LOOP DISCUSSION

Additional details of the procedure used to correct ground loop contamination of pressure measurements are now presented. Pressure signals are measured using Validyne DP15 differential pressure transducers connected to Validyne CD15 Carrier Demodulators. The signals from the Carrier Demodulators are acquired at a rate of 2.0 Hz using a National Instruments NI USB-6210 data acquisition card, connected to the computer workstation. Initially, the pressure signals were always contaminated with significant 60 Hz voltage variations. After some investigation, it was determined that the ground circuit used by the sensitive NI cards and demodulators was contaminated by the large power supplies for the three industrial blowers and the mesh heater. As a result, the pressure signals were spurious and erroneous. To correct this issue, first, a new local ground rod was installed beside the test facility for grounding the sensitive data collection equipment. Second, a 100 microfarad capacitor was installed across the output terminals of each Validyne CD15 Carrier Demodulator. The signals collected after these improvements showed significantly less 60 Hz voltage contamination. All equipment was recalibrated with the new arrangement. Photos of the ground rod and capacitors are included below.

Local ground rod   Demodulator with 100 microfarad capacitor

APPENDIX E

EXPERIMENTAL APPARATUS AND PROCEDURES

Additional details of the apparatus and procedures used in this experiment are now presented.

Test Facility in Propulsion Research Lab at the University of Alabama in Huntsville
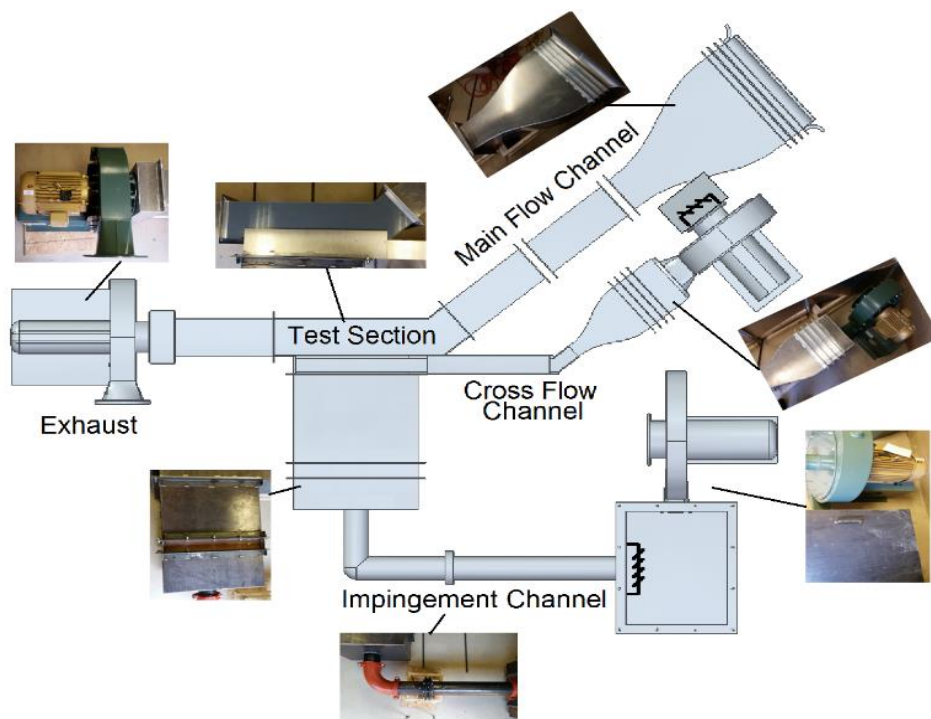
Test Facility with component breakdown

Test Facility with instrumentation layout

Test Facility with controls layout
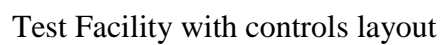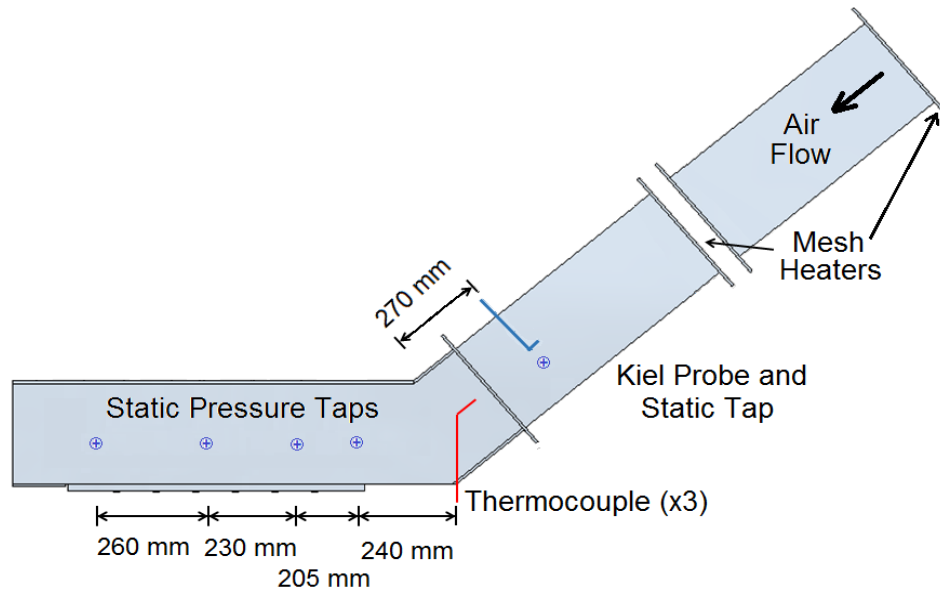
Main flow channel with instrumentation
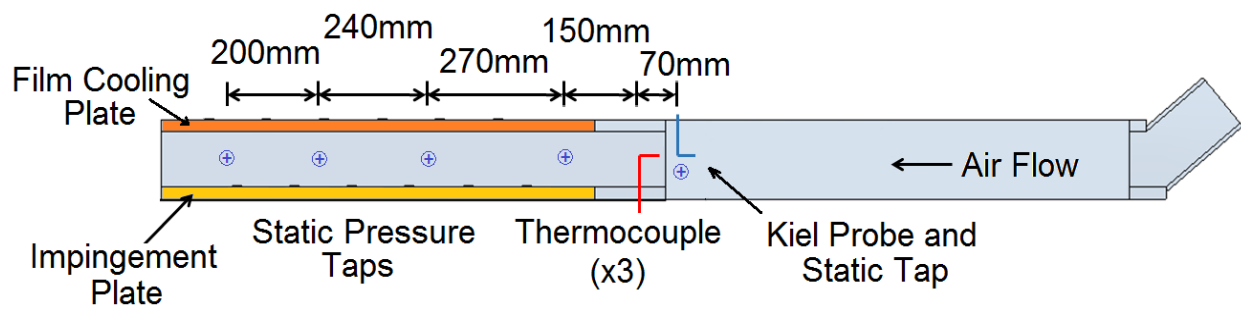
Cross flow channel with instrumentation
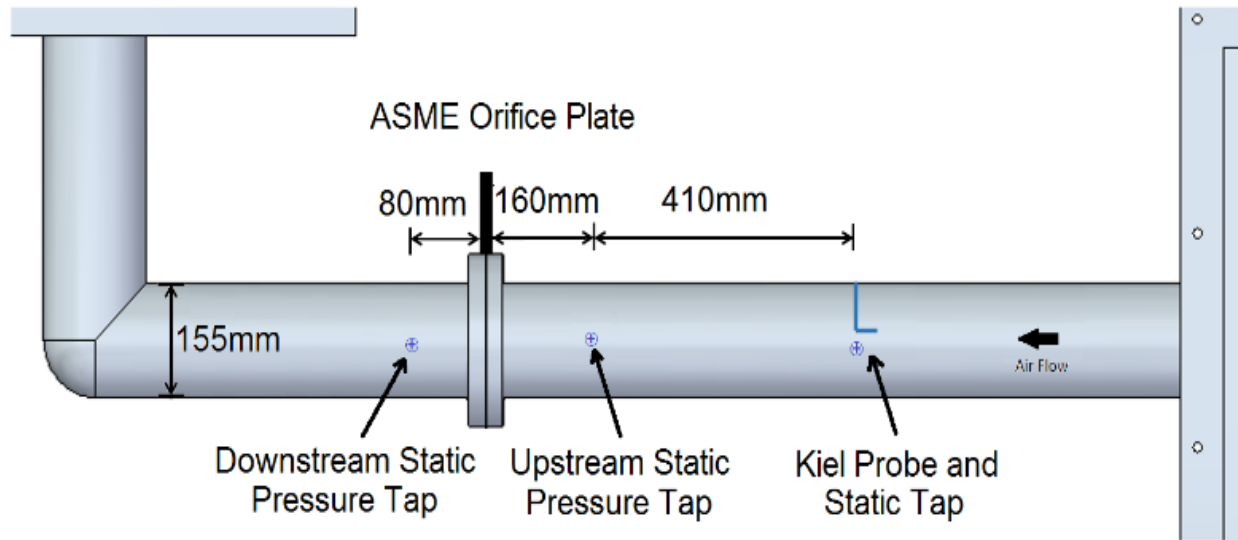
Impingement supply with instrumentation
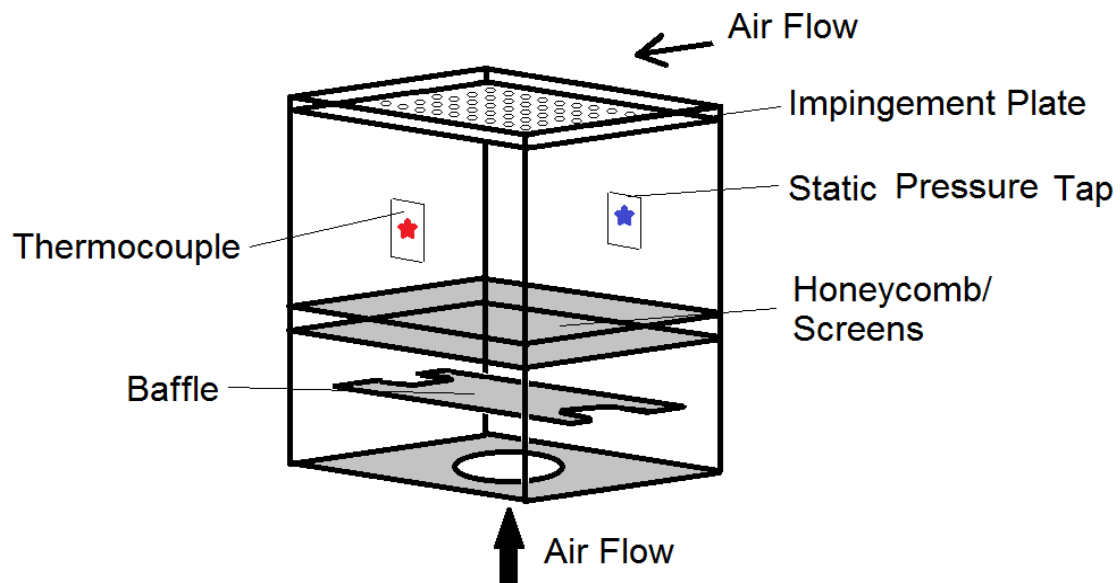
Impingement Plenum with instrumentation
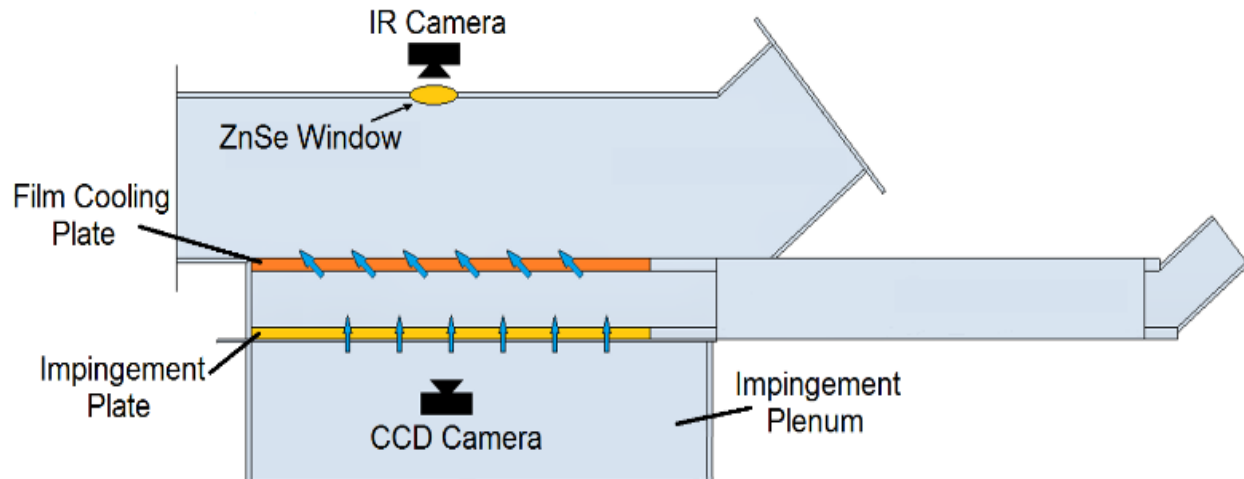
Test section with optical instrumentation

ANALYSIS PROCEDURE

Constants

- Gas constant (R) is a known constant for ambient air ($R = 286.9$ J/kg K)
- Specific heat (c) is a known constant for ambient air ($c = 1005$ J/kg K)
- Specific heat ratio (γ) is a known constant for ambient air ($\gamma = 1.4$)
- Recovery factor (α) is known based on the thermocouple orientation ($\alpha = 0.86$, parallel to flow)
- The reference conditions for Sutherland's Formula are:
    - $C = 120$
    - $T_0 = 291.15$ K
    - $\mu_0 = 1.827$E-5 Pa-s
- Duct cross-sectional area (A_{cs}) and duct hydraulic diameter (D_H) are known for each flow channel
- Orifice area (A_{or}) and diameter ratio (β) are known for the orifice plate ($\beta = 0.5$)
- Impingement hole diameter (d_i), single hole area (A_i), and number of holes (N_i) are known
- Effusion hole diameter (d_e), single hole area (A_e), and number of holes (N_e) are known

Kiel Probe Data Analysis

- There are Kiel Probes in the main flow, the cross flow supply, and the impingement supply channels

- Measured Data:

    - The static pressure taps measure the static pressure (P_s)

    - The Kiel probe and static tap measurement differential is the dynamic pressure (P_d)

    - The thermocouples measure the recovery temperature, (T_r)

- Initially assume $T_s = T_r$

- Static Density: $$\rho_s = P_s/(RT_s)$$

- Local Velocity: $$V = \sqrt{\frac{2P_d}{\rho_s}}$$

- Static temperature: $$T_s = T_r - \alpha * (V^2/2c)$$

- Iterate to correct static temperature (T_s) and velocity (V)

- Mass Flow rate: $$\dot{m} = \rho_s V A_{cs}$$

- Stagnation Temperature: $$T_t = T_s + V^2/2c$$

Southerland's Formula

- Southerland's Formula is used to calculate the dynamic viscosity (μ) of an ideal gas as a function of static temperature (T_s) given a reference condition

- Dynamic Viscosity: $$\mu = \mu_0 \frac{T_0+C}{T_s+C}\left(\frac{T_s}{T_0}\right)^{3/2}$$

- Static Temperature must be given in units of Kelvin

- Dynamic Viscosity will be calculated in units of Pascal-seconds

Orifice Plate

- There is an Orifice plate in the impingement supply channel

- Measured Data:

    - The Static Pressure Taps measure the impingement static pressure ($P_{s,I}$)

    - The Pressure difference across the orifice plate is ΔP_{or}

    - The Thermocouple measurement is converted to impingement static temperature ($T_{s,I}$)

- Impingement dynamic viscosity (μ_I) can be found using Sutherland's formula and $T_{s,I}$

- Initially assume Flow Coefficient (K) to be $K = 0.62$ (a reasonable value)

- Static Density: $$\rho_{s,I} = P_{s,I}/(RT_{s,I})$$

- Mass Flow Rate (Orifice): $\dot{m}_I = K A_{or} \sqrt{2\rho_{s,I}\Delta P_{or}}$

- Reynolds Number: $Re_{or} = \dfrac{\dot{m}_I D_{H,I}}{\mu_I A_{cs,I}}$

- Using Reynolds number and Diameter ratio, a new value for K is found from ASME chart

- Iterate to correct K, $\dot{m}_I$, and Re_{or}

- Average Velocity: $V_I = \dfrac{\dot{m}_I}{\rho_{s,I} A_{cs,I}}$

- This average velocity value should be about 20 percent lower than the Kiel probe centerline velocity

Impingement Plate

- Measured Data:

  - Local static pressure in the effusion supply area ($P_{s,C}$)

  - Static temperature in the plenum ($T_{s,P}$)

  - Average and Local pressure difference across the impingement plate ($\Delta P_{i,Avg}$ and $\Delta P_{i,Local}$)

- Assume velocity in the impingement plenum is approximately zero

  - $T_{s,P} = T_{t,P}$, $P_{s,P} = P_{t,P}$

- Impingement Mass Flow Rate ($\dot{m}_I$) is known from the Orifice Plate Calculation

- Initially assume $T_{s,i} = T_{s,P}$

- Jet Static Density: $\rho_{s,i} = P_{s,C}/(RT_{s,i})$

- Impingement Jet Velocity: $V_i = \dfrac{\dot{m}_I}{\rho_{s,i} A_i N_i}$

- Jet Static Temperature: $T_{s,i} = T_{t,P} - \dfrac{V_i^2}{2c}$

- Iterate to correct $\rho_{s,i}$, V_i, and $T_{s,i}$

- Dynamic viscosity (μ_i) can be found using Sutherland's formula and $T_{s,i}$

- Average Discharge Coefficient: $C_{d,i} = \dfrac{(\rho_{s,i}V_i)_{Avg}}{(\rho_{s,i}V_i)_{Ideal}} = \dfrac{\dot{m}_I/{A_i N_i}}{\sqrt{2\rho_{s,i}(\Delta P_{i,Avg})}}$

- Average Jet Reynolds Number: $Re_{i,Avg} = \dfrac{d_i}{\mu_i}(\rho_{s,i}V_i)_{Avg} = \dfrac{d_i}{\mu_i}\dfrac{\dot{m}_I}{A_i N_i}$

- Average Mach Number: $M_{i,Avg} = \dfrac{V_{i,Avg}}{\sqrt{\gamma RT_{s,i}}} = \dfrac{V_i}{\sqrt{\gamma RT_{s,i}}}$

- Local values can be found using local static pressure drop across the plate

- Local Jet Reynolds Number: $Re_{i,Local} = \dfrac{d_i}{\mu_i}(\rho_{s,i}V_i)_{Local} = \dfrac{d_i}{\mu_i}C_{d,i}\sqrt{2\rho_{s,i}\Delta P_{i,Local}}$

- Local Mach Number: $M_{i,Local} = \dfrac{V_{i,Local}}{\sqrt{\gamma RT_{s,i}}} = \dfrac{C_{d,i}\sqrt{2\Delta P_{i,Local}}}{\sqrt{\rho_{s,i}}\sqrt{\gamma RT_{s,i}}}$

Effusion Plate

- Measured Data:
    - Local static pressure in the main flow area ($P_{S,M}$)
    - Average and Local pressure difference across the effusion plate ($\Delta P_{e,Avg}$ and $\Delta P_{e,Local}$)
- Cross flow and Impingement Mass Flow Rates ($\dot{m}_C$ and $\dot{m}_I$ respectively) are known from previous calculations
- Cross flow and Impingement Stagnation Temperatures ($T_{t,C}$ and $T_{t,I}$ respectively) are known from previous calculations
- Mass Flow Rate (Effusion): $\qquad \dot{m}_e = \dot{m}_C + \dot{m}_I$
- Effusion Static Temperature: $\qquad T_{t,e} = \dfrac{T_{t,C}\dot{m}_C + T_{t,I}\dot{m}_I}{\dot{m}_e}$
- Initially assume $T_{t,e} = T_{s,e}$
- Jet Static Density: $\qquad \rho_{s,e} = P_{S,M}/(RT_{s,e})$
- Effusion Hole Velocity: $\qquad V_e = \dfrac{\dot{m}_e}{\rho_{s,e}A_e N_e}$
- Jet Static Temperature: $\qquad T_{s,e} = T_{t,e} - \dfrac{V_e^2}{2c}$
- Iterate to correct $\rho_{s,e}$, V_e, and $T_{s,e}$
- Dynamic viscosity (μ_e) can be found using Sutherland's formula and $T_{s,e}$
- Average Discharge Coefficient: $\qquad C_{d,e} = \dfrac{(\rho_{s,e}V_e)_{Avg}}{(\rho_{s,e}V_e)_{Ideal}} = \dfrac{\dot{m}_e/A_e N_e}{\sqrt{2\rho_{s,e}(\Delta P_{e,Avg})}}$
- Average Blowing Ratio: $\qquad BR_{e,Avg} = \dfrac{(\rho_{s,e}V_e)_{Avg}}{(\rho_{s,M}V_M)_{Avg}} = \dfrac{\dot{m}_e/A_e N_e}{\rho_{s,M}V_M}$
- Average Jet Reynolds Number: $\qquad Re_{e,Avg} = \dfrac{d_e}{\mu_e}\left(\rho_{s,e}V_e\right)_{Avg} = \dfrac{d_e}{\mu_e}\dfrac{\dot{m}_e}{A_e N_e}$
- Average Mach Number: $\qquad M_{e,Avg} = \dfrac{V_{e,Avg}}{\sqrt{\gamma RT_{s,e}}} = \dfrac{\dot{m}_e/\rho_{s,e}A_e N_e}{\sqrt{\gamma RT_{s,e}}}$
- Local values can be found using local static pressure drop across the plate
- Local dynamic pressure: $\qquad P_{d,M,Local} = P_{t,M} - P_{s,M,Local}$
- Local Blowing Ratio: $\qquad BR_{e,Local} = \dfrac{(\rho_{s,e}V_e)_{Local}}{(\rho_{s,M}V_M)_{Local}} = \dfrac{C_{d,e}\sqrt{2\rho_{s,e}\Delta P_{e,Local}}}{\sqrt{2\rho_{s,M}P_{d,M,Local}}}$
- Local Jet Reynolds Number: $\qquad Re_{e,Local} = \dfrac{d_e}{\mu_e}\left(\rho_{s,e}V_e\right)_{Local} = \dfrac{d_e}{\mu_e}C_{d,e}\sqrt{2\rho_{s,e}\Delta P_{e,Local}}$
- Local Mach Number: $\qquad M_{e,Local} = \dfrac{V_{e,Local}}{\sqrt{\gamma RT_{s,e}}} = \dfrac{C_{d,e}\sqrt{2\Delta P_{e,Local}}}{\sqrt{\rho_{s,e}}\sqrt{\gamma RT_{s,e}}}$

APPENDIX F

SOFTWARE DIRECTORY

A listing of software by filename, with a brief description of its use in this thesis now follows.

Software	File Name	Description
LabView	Facility Measurements v7 (Crossflow).vi	LabView program used to collect and store raw flow condition data from thermocouples and pressure transducers
Flir ResearchIR	N/A	Used to collect and store infrared images from the infrared camera
Excel	Flow Measurements, Format v8.xlsx	Used to calculate flow parameters from LabView output
Excel	Thermocouple Readings, Format v4.xlsx	Used to plot temperature data from LabView output
MATLAB	AAA_IR_Transient_Analysis_v7.m	Used to generate matrices of heat transfer data from infrared video data
MATLAB	BBB_IR_Transient_Plots_v7.m	Used to generate plots of results from matrices of heat transfer data
MATLAB	comparison_plots.m	Used to generate plots of results from matrices of heat transfer data

APPENDIX G

DATA FILE DIRECTORY

A listing of data files by filename now follows. These data files include both the raw and reduced data files for the results presented in this thesis defense.

Main Flow Velocity	Blowing Ratio	Data File name	Description
5.1 m/s	3.62	Flow Data, A.txt	Raw output from LabView, containing pressure and temperature data
		Temperatures, A.txt	Raw output from LabView, containing temperature data
		Flow Measurements, 11-06-2015A.xlsx	Excel file used to calculate flow data from Flow Data, A.txt file
		Thermocouple Readings, 11-06-2015A.xlsx	Excel file used to plot transient temperature data from Temperatures, A.txt file
		11-06-2015 A.seq	Raw output from Flir ResearchIR software containing all infrared data from the infrared camera
		11-06-2015 A 19 to 29.wmv	Grayscale video output from ResearchIR software with linear temperature scale
		11-06-2015 A 19 to 29.mat	Output from MATLAB program, which contains the calculated matrices of transient, spatially-resolved heat transfer data
5.00 m/s	4.37	Flow Data, B.txt	Raw output from LabView, containing pressure and temperature data
		Temperatures, B.txt	Raw output from LabView, containing temperature data
		Flow Measurements, 11-06-2015B.xlsx	Excel file used to calculate flow data from Flow Data, B.txt file

		Thermocouple Readings, 11-06-2015B.xlsx	Excel file used to plot transient temperature data from Temperatures, B.txt file
		11-06-2015 B.seq	Raw output from Flir ResearchIR software containing all infrared data from the infrared camera
		11-06-2015 B 20 to 30.wmv	Grayscale video output from ResearchIR software with linear temperature scale
		11-06-2015 B 20 to 30.mat	Output from MATLAB program, which contains the calculated matrices of transient, spatially-resolved heat transfer data
5.04 m/s	**4.09**	Flow Data, C.txt	Raw output from LabView, containing pressure and temperature data
		Temperatures, C.txt	Raw output from LabView, containing temperature data
		Flow Measurements, 11-06-2015C.xlsx	Excel file used to calculate flow data from Flow Data, C.txt file
		Thermocouple Readings, 11-06-2015C.xlsx	Excel file used to plot transient temperature data from Temperatures, C.txt file
		11-06-2015 C.seq	Raw output from Flir ResearchIR software containing all infrared data from the infrared camera
		11-06-2015 C 20 to 30.wmv	Grayscale video output from ResearchIR software with linear temperature scale
		11-06-2015 C 20 to 30.mat	Output from MATLAB program, which contains the calculated matrices of transient, spatially-resolved heat transfer data
4.94 m/s	**4.94**	Flow Data, D.txt	Raw output from LabView, containing pressure and temperature data
		Temperatures, D.txt	Raw output from LabView, containing temperature data

		Flow Measurements, 11-06-2015D.xlsx	Excel file used to calculate flow data from Flow Data, D.txt file
		Thermocouple Readings, 11-06-2015D.xlsx	Excel file used to plot transient temperature data from Temperatures, D.txt file
		11-06-2015 D.seq	Raw output from Flir ResearchIR software containing all infrared data from the infrared camera
		11-06-2015 D 21 to 31.wmv	Grayscale video output from ResearchIR software with linear temperature scale
		11-06-2015 D 21 to 31.mat	Output from MATLAB program, which contains the calculated matrices of transient, spatially-resolved heat transfer data
7.18 m/s	**3.06**	Flow Data, E.txt	Raw output from LabView, containing pressure and temperature data
		Temperatures, E.txt	Raw output from LabView, containing temperature data
		Flow Measurements, 11-06-2015E.xlsx	Excel file used to calculate flow data from Flow Data, E.txt file
		Thermocouple Readings, 11-06-2015E.xlsx	Excel file used to plot transient temperature data from Temperatures, E.txt file
		11-06-2015 E.seq	Raw output from Flir ResearchIR software containing all infrared data from the infrared camera
		11-06-2015 E 21 to 31.wmv	Grayscale video output from ResearchIR software with linear temperature scale
		11-06-2015 E 21 to 31.mat	Output from MATLAB program, which contains the calculated matrices of transient, spatially-resolved heat transfer data
7.13 m/s	**3.32**	Flow Data, F.txt	Raw output from LabView, containing pressure and temperature data

		Temperatures, F.txt	Raw output from LabView, containing temperature data
		Flow Measurements, 11-06-2015F.xlsx	Excel file used to calculate flow data from Flow Data, F.txt file
		Thermocouple Readings, 11-06-2015F.xlsx	Excel file used to plot transient temperature data from Temperatures, F.txt file
		11-06-2015 F.seq	Raw output from Flir ResearchIR software containing all infrared data from the infrared camera
		11-06-2015 F 21 to 31.wmv	Grayscale video output from ResearchIR software with linear temperature scale
		11-06-2015 F 21 to 31.mat	Output from MATLAB program, which contains the calculated matrices of transient, spatially-resolved heat transfer data
7.08 m/s	**3.63**	Flow Data, G.txt	Raw output from LabView, containing pressure and temperature data
		Temperatures, G.txt	Raw output from LabView, containing temperature data
		Flow Measurements, 11-06-2015G.xlsx	Excel file used to calculate flow data from Flow Data, G.txt file
		Thermocouple Readings, 11-06-2015G.xlsx	Excel file used to plot transient temperature data from Temperatures, G.txt file
		11-06-2015 G.seq	Raw output from Flir ResearchIR software containing all infrared data from the infrared camera
		11-06-2015 G 21 to 31.wmv	Grayscale video output from ResearchIR software with linear temperature scale
		11-06-2015 G 21 to 31.mat	Output from MATLAB program, which contains the calculated matrices of transient, spatially-resolved heat transfer data

7.02 m/s	3.90	Flow Data, H.txt	Raw output from LabView, containing pressure and temperature data
		Temperatures, H.txt	Raw output from LabView, containing temperature data
		Flow Measurements, 11-06-2015H.xlsx	Excel file used to calculate flow data from Flow Data, H.txt file
		Thermocouple Readings, 11-06-2015H.xlsx	Excel file used to plot transient temperature data from Temperatures, H.txt file
		11-06-2015 H.seq	Raw output from Flir ResearchIR software containing all infrared data from the infrared camera
		11-06-2015 H 22 to 32.wmv	Grayscale video output from ResearchIR software with linear temperature scale
		11-06-2015 H 22 to 32.mat	Output from MATLAB program, which contains the calculated matrices of transient, spatially-resolved heat transfer data
9.22 m/s	2.78	Flow Data, I.txt	Raw output from LabView, containing pressure and temperature data
		Temperatures, I.txt	Raw output from LabView, containing temperature data
		Flow Measurements, 11-06-2015I.xlsx	Excel file used to calculate flow data from Flow Data, I.txt file
		Thermocouple Readings, 11-06-2015I.xlsx	Excel file used to plot transient temperature data from Temperatures, I.txt file
		11-06-2015 I.seq	Raw output from Flir ResearchIR software containing all infrared data from the infrared camera
		11-06-2015 I 22 to 32.wmv	Grayscale video output from ResearchIR software with linear temperature scale

		11-06-2015 I 22 to 32.mat	Output from MATLAB program, which contains the calculated matrices of transient, spatially-resolved heat transfer data
9.18 m/s	**2.96**	Flow Data, J.txt	Raw output from LabView, containing pressure and temperature data
		Temperatures, J.txt	Raw output from LabView, containing temperature data
		Flow Measurements, 11-06-2015J.xlsx	Excel file used to calculate flow data from Flow Data, J.txt file
		Thermocouple Readings, 11-06-2015J.xlsx	Excel file used to plot transient temperature data from Temperatures, J.txt file
		11-06-2015 J.seq	Raw output from Flir ResearchIR software containing all infrared data from the infrared camera
		11-06-2015 J 23 to 33.wmv	Grayscale video output from ResearchIR software with linear temperature scale
		11-06-2015 J 23 to 33.mat	Output from MATLAB program, which contains the calculated matrices of transient, spatially-resolved heat transfer data
9.13 m/s	**3.12**	Flow Data, K.txt	Raw output from LabView, containing pressure and temperature data
		Temperatures, K.txt	Raw output from LabView, containing temperature data
		Flow Measurements, 11-06-2015K.xlsx	Excel file used to calculate flow data from Flow Data, K.txt file
		Thermocouple Readings, 11-06-2015K.xlsx	Excel file used to plot transient temperature data from Temperatures, K.txt file
		11-06-2015 K.seq	Raw output from Flir ResearchIR software containing all infrared data from the infrared camera

		11-06-2015 K 23 to 33.wmv	Grayscale video output from ResearchIR software with linear temperature scale
		11-06-2015 K 23 to 33.mat	Output from MATLAB program, which contains the calculated matrices of transient, spatially-resolved heat transfer data
9.08 m/s	**3.30**	Flow Data, L.txt	Raw output from LabView, containing pressure and temperature data
		Temperatures, L.txt	Raw output from LabView, containing temperature data
		Flow Measurements, 11-06-2015L.xlsx	Excel file used to calculate flow data from Flow Data, L.txt file
		Thermocouple Readings, 11-06-2015L.xlsx	Excel file used to plot transient temperature data from Temperatures, L.txt file
		11-06-2015 L.seq	Raw output from Flir ResearchIR software containing all infrared data from the infrared camera
		11-06-2015 L 24 to 34.wmv	Grayscale video output from ResearchIR software with linear temperature scale
		11-06-2015 L 24 to 34.mat	Output from MATLAB program, which contains the calculated matrices of transient, spatially-resolved heat transfer data

REFERENCES

[1] Ligrani, P. M., Goodro, M., Fox, M., and Moon, H.-K., 2015, "Full-Coverage Film Cooling: Heat Transfer Coefficients and Film Effectiveness For a Sparse Hole Array at Different Blowing Ratios and Contraction Ratios," ASME Transactions-Journal of Heat Transfer, Vol. 137(3), pp. 032201-1 to 032201-12.

[2] Ligrani, P. M., Goodro, M., Fox, M., and Moon, H.-K., 2012, "Full-Coverage Film Cooling: Film Effectiveness and Heat Transfer Coefficients For Dense and Sparse Hole Arrays at Different Blowing Ratios," ASME Transactions-Journal of Turbomachinery, 134(6), pp. 061039-1 to 061039-13.

[3] Lee, J., Ren, Z., Ligrani, P. M., Lee, D. H., Fox, M., Moon, H.-K., 2014, "Cross-Flow Effects on Impingement Array Heat Transfer With Varying Jet-To-Target Plate Distance and Hole Spacing," International Journal of Heat and Mass Transfer, 75, pp. 534-544.

[4] Scrittore, J. J., Thole, K. A., and Burd, S. W., 2007, "Investigation of Velocity Profiles for Effusion Cooling of a Combustor Liner," ASME Transactions - Journal of Turbomachinery, 129, pp. 518-526.

[5] Baldauf S., Schultz A., and Wittig S., 2001, "High-Resolution Measurements of Local Effectiveness From Discrete Hole Film Cooling," ASME Transactions - Journal of Turbomachinery, 123, pp. 758-765.

[6] Baldauf S., Schultz A., and Wittig S., 2001, "High-Resolution Measurements of Local Heat Transfer Coefficients From Discrete Hole Film Cooling," ASME Transactions - Journal of Turbomachinery, 123, pp. 749-757.

[7] Bell, C. M., Hamakawa, H., and Ligrani, P. M., 2000, "Film Cooling from Shaped Holes," ASME Transactions-Journal of Heat Transfer, 122 (2), pp. 224-232.

[8] Yuen, C. H. N., and Martinez-Botas, R. F., 2005, "Film Cooling Characteristics of Row of Round Holes at Various Streamwise Angles in a Crossflow: Part I. Effectiveness," International Journal of Heat and Mass Transfer, 48, pp. 4995-5016.

[9] Coulthard, S. M., Volino, R. J., and Flack, K. A., 2006, "Effect of unheated Starting Lengths on Film Cooling Experiments," ASME Transactions - Journal of Turbomachinery, 128, pp. 579-588.

[10] Saumweber, C., and Schulz, A., 2004, "Interaction of Film Cooling Rows: Effects of Hole Geometry and Row Spacing on the Cooling Performance Downstream of the Second Row of Holes," ASME Transactions - Journal of Turbomachinery, 126, pp. 237-246.

[11] Chappell, J., Ligrani, P. M., Sreekanth, S., Lucas, T., and E. Vlasic, 2010, "Aerodynamic Performance of Suction-Side Gill-Region Film Cooling," ASME Transactions-Journal of Turbomachinery, 132(3), pp. 031020-1 to 031020-11.

[12] Chappell, J., Ligrani, P. M., Sreekanth, S., and Lucas, T., 2010, "Suction-Side Gill-Region Film Cooling: Effects of Hole Shape and Orientation on Adiabatic Effectiveness and Heat Transfer Coefficient," ASME Transactions-Journal of Turbomachinery, 132(3), pp. 031022-1 to 031022-11.

[13] Lin, Y., Song, B., Li, B., Liu, G., and Wu, Z., 2003, "Investigation of Film Cooling Effectiveness of Full-Coverage Inclined Multihole Walls with Different Hole Arrangements," ASME Paper Number GT-2003-38881.

[14] Schulz, A., 2001, "Combustor Liner Cooling Technology in Scope of Reduced Pollulant Formation and Rising Thermal Efficiencies," Heat Transfer in Gas Turbine Systems (Editor: R. J. Goldstein), Annals of the New York Academy of Sciences: New York, 934, pp. 135-146.

[15] Bailey, J. C., Intile, J., Tolpadi, A., Fric, T., Nirmalan, N. V., and Bunker, R. S., 2002, "Experimental and Numerical Study of Heat Transfer in a Gas Turbine Combustor Liner," ASME Transactions – Journal of Engineering for Gas Turbines and Power, 125(5), pp.994-1002.

[16] Amano, R. S., 2008, "Advances in Gas Turbine Blade Cooling Technology," Advanced Computational Methods and Experiments in Heat Transfer X (Editors: B. Sunden, C. A. Brebbia), WIT Press, Southampton.

[17] Bunker, R. S., 2008, "Innovative Gas Turbine Cooling Techniques," Thermal Engineering in Power Systems (Editors: R. S. Amano, B. Sunden), WIT Press, Southampton.

[18] Cho, H. H., Rhee, D. H., 2001, "Local heat/mass transfer measurement on the effusion plate in impingement/effusion cooling systems," ASME

[19] King, A., Jagannatha, D., 2009, "Simulation of synthetic jets with non-sinusoidal forcing functions for heat transfer applications," The 18th World IMACS Congress and MODSIM09 International Congress on Modelling and Simulation

[20] Kumar, S., Amano, R. S., Lucci, J. M., 2013, "Numerical simulations of heat transfer distribution of a two-pass square channel with V-rib turbulator and bleed holes," Journal of Heat and Mass Transfer, Volume 49, Issue 8 , pp 1141-1158

[21] Barigozzi, G., Benzoni, G., Franchini, G., and Perdichizzi, A., 2006, "Fan-Shaped Hole Effects on the Aero-Thermal Performance of a Film-Cooled Endwall," ASME Transactions - Journal of Turbomachinery, 128, pp. 43-51.

[22] Oldfield, M. L. G., 2008, "Impulse Response Processing of Transient Heat Transfer Gauge Signals, ASME Transactions-Journal of Turbomachinery, 130(2), pp. 021023-1 to 021023-9.

[23] O'Dowd, D., Zhang, Q., He, L., Ligrani, P. M., and Friedrichs, S., 2011, "Comparison of Heat Transfer Measurement Techniques on a Transonic Turbine Blade Tip," ASME Transactions-Journal of Turbomachinery, 133 (2) pp. 021028-1 to 021028-10.

[24] Anthony, R. J., Oldfiend, M. L. G., Jones, T. V., and LaGraff, J. E., 1999, "Development of High-Density Arrays of Thin Film Heat Transfer Gauges," JSME Thermal Engineering Joint Conference AJTE99-6159.

[25] Kline, S. J., and McClintock, F. A., 1953, "Describing Uncertainties in Single Sample Experiments," Mechanical Engineering, 75, pp. 3-8.

[26] Moffat, R. J., 1988, "Describing the Uncertainties in Experimental Results," Experimental Thermal and Fluid Science, 1(1), pp. 3-17.

[27] Gritsch, M., Schulz, A., and Wittig, S., 2001, "Effect of Crossflows on the Discharge Coefficient of Film Cooling Holes with Varying Angles of Inclination and Orientation," ASME Transactions - Journal of Turbomachinery, 123, pp. 781-787.

[28] Kline, S. J., and McClintock, F. A., 1953, "Describing Uncertainties in Single Sample Experiments," Mechanical Engineering, 75, pp. 3-8.

[29] Moffat, R. J., 1988, "Describing the Uncertainties in Experimental Results," Experimental Thermal and Fluid Science,1 (1), pp. 3-17.

[30] Rogers, N., Ren, Z., Buzzard, W., Tinker, N., Sweeney, B., Ligrani, P., Hollingsworth, K., Liberatore, F., Patel, R., Moon, H-K., 2016, "Effects of Double Wall Cooling Configuration and Conditions on Performance of Full Coverage Effusion Cooling," Proceedings of ASME Turbo Expo 2016: Turbomachinery Technical Conference and Exposition, June 13-17, 2016, Seoul, South Korea, GT2016-56515